目　次

1. 主論文

Ferroquadrupolar ordering in UCu_2Sn
(UCu_2Sn における強四重極子秩序)

石井　勲

2. 公表論文

(1) Spontaneous strain due to ferroquadrupolar ordering in UCu_2Sn
I. Ishii , H. Higaki , K. Katoh , T. Takabatake , H. Goshima , T. Fujita , T. Suzuki
Physical Review B **68**, 144413(4) (2003).

(2) Thermal expansion of UCu_2Sn in the basal plane
I. Ishii , H. Higaki , K. Katoh , T. Takabatake , H. Goshima , T. Fujita , T. Suzuki
Physica B **329-333**, 553-554 (2003).

3. 参考論文

(1) Elastic anomaly of UCu_2Sn in the magnetic fields
T. Suzuki , I. Ishii , N. Okuda , K. Katoh , T. Takabatake , T. Fujita , A. Tamaki
Journal of Magnetism and Magnetic Materials **226-230**, 983-984 (2001).

(2) Quadrupolar ordering of 5*f* electrons in UCu_2Sn
T. Suzuki , I. Ishii , N. Okuda , K. Katoh , T. Takabatake , T. Fujita , A. Tamaki
Physical Review B **62**, 49-52 (2000).

(3) Jahn-Teller instability in a ternary uranium compound
T. Suzuki , I. Ishii , N. Okuda , K. Katoh , T. Takabatake , T. Fujita , A. Tamaki
Physica B **284-288**, 1301-1302 (2000).

(4) Elastic quantum oscillation of LuB_{12}
N. Okuda , T. Suzuki , I. Ishii , S. Hiura , F. Iga , T. Takabatake , T. Fujita ,
H. Kadomatsu , H. Harima
Physica B **281&282**, 756-757 (2000).

主　論　文

Abstract

The ternary uranium compound UCu_2Sn with a hexagonal $ZrPt_2Al$-type structure shows a phase transition at 16 K. We reported previously that huge lattice-softening is accompanied by the phase transition, which originates from ferroquadrupolar ordering of the ground state non-Kramers doublet Γ_5. However, the electronic entropy in UCu_2Sn was not reproduced by the entropy calculated from that CEF level scheme. We measured the elastic modulus C_{66} in the magnetic field parallel to [100], [001] and [110] by the phase-comparison type pulse-echo method and made out the $H-T$ phase diagram of UCu_2Sn. So, we optimized the CEF parameters so as to reproduce the data of entropy, magnetic susceptibility, elastic moduli and C_{66} in the magnetic field parallel to [100], [001] and [110]. The proposed level scheme is the ground state doublet Γ_5, the first excited state Γ_4 at 109 K and $\cdots$. The $H-T$ phase diagram is well reproduced. A macroscopic strain, which is expected to emerge spontaneously, was not detected by powder X-ray diffraction in the temperature range between 4.2 and 300 K. To search the spontaneous strain, we have manufactured the capacitance cell and carried out thermal expansion measurements on a single-crystalline sample along the a, b and c axes using a capacitance technique with the resolution of 10^{-8}. We found the spontaneous $\varepsilon_{xx}-\varepsilon_{yy}$ strain which couples to the ground state doublet Γ_5. The effect of uniaxial pressure along the a, b and c axes on the transition temperature is also discussed.

Contents

Chapter 1

Introduction

1.1 Orbital flexibility

The electron on each orbit moves in a electric charge distribution depended on the orbit. A wave function of s, p, d and f orbits are shown in Fig. 1. s orbit which is a orbital angular momentum $L = 0$ is expressed as scalar, that is the monopole. p orbit which is $L = 1$ is expressed as vector, that is the dipole, and d orbit which is $L = 2$ is expressed as second-order tensor, that is the quadrupole. f orbit which is $L = 3$ is expressed as third-order tensor, that is the octopole. The orbit which has a multipole higher than a quadrupole is d and f orbits. A symmetry of electron on the orbit is lowered by a crystal electric field (CEF) from other ligands depended on the crystal structure. In f electron systems, few high symmetry compounds, such as a cubic, have a octopole. In a hexagonal symmetry, thereto, some compounds have a quadrupole at the highest. Multipoles which have such a electric charge distribution arranged in parallel and anti-parallel with each other are called as ferromultipolar and anti-ferromultipolar ordering. In ferroquadrupolar ordering, quadrupole couples to strain which is the second-order tensor and the crystal symmetry lowers.

A flexibility of an electric charge and a spin, which are related to the electric conduction and the magnetism for instance, respectively, are considered mainly so far in solid state properties. Recently, a orbital flexibility is attracted in addition to the electric charge flexibility and the spin flexibility. Extensive searches have been carried out for the interaction between the spin flexibility and the orbital flexibility and among the orbital flexibility. In d electron systems, many compounds, such as a

perovskite-type Mn oxides, are reported to show the order of orbital flexibility. The perovskite-type Mn oxides have been applied to a magnetic device by using a colossal magnetoresistance derived from the orbital flexibility. The orbital angular momentum L is quenched in the d electron systems which have the itinerant property. CEF effect is relatively stronger than a spin-orbital interaction. The Jahn-Teller interaction which is a interaction between a strain and multipole is mainly affected to order in d electron systems. In $4f$ electron systems, many compounds, such as CeB_6, are reported to show the order of orbital flexibility [1]. In case of a localized f electron state in $4f$ electron systems, the total angular momentum J is good quantum number according to the spin-orbit interaction which is relatively stronger than CEF. The multipole-multipole interaction is mainly affected to order in $4f$ electron systems. In $5f$ electron systems, a few compounds, including NpO_2 [2], UPd_3 [3], URu_2Si_2 [4], UNiSn [5] and UCu_2Sn [6], are reported to show the multipolar ordering. $5f$ electrons have an intermediate property between the strongly localized property of $4f$ electrons and the itinerant property of d electrons. Shown in Fig. 2 [7], $5f$ electrons mainly exist in the inside of $6s$ and $6p$ orbits as for spatial spread of the U wave function. However, $5f$ electrons have a certain probability of existence also in the outside of these orbits. Studies of the multipolar ordering in $5f$ electron systems which connect between d and $4f$ electron systems are useful to an understanding of the multipolar ordering as whole the strongly correlated electron system.

1.2 UCu_2Sn

The ternary uranium compound UCu_2Sn has a hexagonal $ZrPt_2Al$-type structure (space group $P6_3/mmc$) shown in Fig. 3. U, Cu and Sn atoms are located in (1/3, 2/3, 1/4), (1/3, 2/3, 0.58) and (0, 0, 0) atomic site, respectively. Lattice parameters are $a = 4.457$ Å and $c = 8.713$ Å at room temperature. All constituent atoms are stacked in layers perpendicular to the hexagonal c-axis with a sequence of $\cdots$Sn, Cu, U and Cu$\cdots$. U atoms in UCu_2Sn which have a single U site form a triangular lattice. A distance between U layer and Cu layers of upper and lower sides is unequivalent though a distance between U layer and Sn layers is equivalent. The

nearest interatomic distance between U and U, Cu and Sn are $d_{\mathrm{U-U}} = 4.46$ Å , $d_{\mathrm{U-Cu}} = 2.87$ Å and $d_{\mathrm{U-Sn}} = 3.37$ Å , respectively [8]. It is thought that a influence by the overlap between $5f$ electron wave functions of U is small since $d_{\mathrm{U-U}} >$ Hill limit [9].

Takabatake *et al.* found that UCu_2Sn underwent a phase transition around 16 K [10]. Figure 4 shows the temperature dependence of specific heat for instance. At first, the transition was considered as an antiferromagnetic ordering because cusp-like behavior was seen at 16 K in the magnetic susceptibility shown in Fig.5 and spin-flop-like change in the magnetization curve was also observed at 23.5 T in the ordered state shown in Fig.6 [11]. As for the electrical resistivity shown in Fig. 7, a rapid increase below 16 K was considered as an influence caused by development of the superzone gap [11]. However, the transition was estimated to be a non-magnetic one since Mössbauer [12] and NMR [13] (Fig. 8) spectroscopies inferred the absence of a hyperfine field at Sn and Cu sites and neutron diffraction detected no magnetic reflection [11] in the ordered state. In Muon Spin Resonance (μSR) measurement, furthermore, no change was detected in muon spin relaxation between above and below 16 K [14].

We estimated a entropy derived from electrons in UCu_2Sn, which subtracted the specific heat caused by a lattice contribution of reference compound $ThCu_2Sn$ from the data of UCu_2Sn, shown by solid circles in inset of Fig. 4. The electronic entropy in UCu_2Sn is about $R \ln 2$ at 16 K, where R is gas constant. The ground state of CEF in non-ordered state is considered as a doublet. The magnetic susceptibility of UCu_2Sn above 150 K shows the Curie-Weiss behavior with an effective magnetic moment of $\mu_{\mathrm{eff}} = 3.0 \sim 3.6 \mu_{\mathrm{B}}$/U corresponding to $5f^2$ or $5f^3$ configurations, which suggests the localized property of $5f$ electrons above 150 K. If $5f$ electrons in UCu_2Sn have the $5f^2$ configuration with the total angular momentum $\boldsymbol{J} = 4$ and nearly localized property through to low temperatures, a ground multiplet of $5f$ electrons in hexagonal CEF splits into seven eigen-states; three singlets Γ_1, Γ_3 and Γ_4, and three non-Kramers doublets $2\Gamma_5$ and Γ_6 with degenerate quadrupoles, where Γ_i denotes the irreducible representation for the 6/mmm point group. Therefore, we expected that the ground state of UCu_2Sn is non-Kramers doublet which have a

quadrupole degeneracy.

If f electrons have a quadrupole moment, a strain induced by the ultrasonic linearly couples to these quadrupole moment and the elastic modulus corresponding to a symmetry of quadrupole moment shows a softening. We measured elastic moduli which are a good probe for observation of a lattice change. In Fig. 9, a large softening with more than 56 % reduction at 16 K was observed in the temperature dependence of elastic modulus C_{66} [6], which is an evidence for the quadrupolar ordering of the ground state Γ_5. Taking account of both the strain-quadrupole coupling and the quadrupole-quadrupole (q-q) coupling, we analyzed C_{66} and then obtained the positive sign for the q-q coupling coefficient g'_{Γ_5}, that is, ferroquadrupolar coupling in the ground state. To distinguish the quadrupolar ordering from the cooperative Jahn-Teller transition, we employed a non-dimensional parameter $D \equiv \mid g'C_0/g^2\mathrm{N}_0 \mid$ [15], where g is the strain-quadrupole coupling constant, C_0 is the background stiffness and N_0 is the number density of U ions per unit volume at room temperature. The obtained result $D \gg 1$ clearly indicated that the q-q coupling g' predominates over the strain-quadrupole coupling g in UCu_2Sn and consequently the transition is classified as the ferroquadrupolar ordering. The prominent result of above work was finding of the phase transition in UCu_2Sn caused by quadrupole degeneracy of the ground state doublet Γ_5. The level scheme of CEF which is most reproducible for elastic moduli is shown in inset of Fig. 9. However, the electronic entropy in UCu_2Sn was not reproduced by the entropy calculated from the CEF level scheme shown in inset of Fig. 4.

Chapter 2

Purpose

To investigate the ordered state in UCu_2Sn and make out the $H-T$ phase diagram, We have measured the elastic modulus C_{66} in the magnetic field parallel to [100], [001] and [110]. We have also optimized the CEF parameters so as to reproduce the data of entropy, magnetic susceptibility, elastic moduli and C_{66} in the magnetic field parallel to [100], [001] and [110].

The ferroquadrupolar ordering must be accompanied by a macroscopic strain or distortion below T_Q. To observe the spontaneous strain, we have carried out the X-ray diffraction experiment on a polycrystalline sample. Thereto, we have manufactured the capacitance cell and carried out thermal expansion measurements on a single-crystalline sample along the a, b and c axes using the sensitive three-terminal capacitance method with higher resolution $\sim 10^{-8}$.

Chapter 3

Experimental

3.1 Samples

A single crystal of UCu_2Sn was grown by a Bridgman method. The details of sample preparation was described elsewhere [11]. Electron Probe Micro Analysis for our single-crystalline sample of UCu_2Sn detected the impurity phase of UCuSn at $\sim$ 4 % of the host crystal. The dimensions of the sample is $2.824 \times 2.908 \times 3.288$ mm^3. Each plane was polished by number 800, 3000 carborundum and ϕ 0.05 μm alumina powder so as to shape into a rectangular parallelepiped. A powdered sample of UCu_2Sn for X-ray diffraction experiments was prepared from the polycrystal of UCu_2Sn. These samples were provided by Takabatake laboratory, Department of Quantum Matter, ADSM, Hiroshima University.

3.2 Ultrasonic measurements

3.2.1 Phase-comparison type pulse-echo method

The elastic modulus is given by the following relation:

$$C = \rho v^2 \tag{3.1}$$

where ρ is a mass density and v is a propagation velocity. We disregarded a temperature dependence of ρ and applied the value of $\rho = 10.72$ (g / cm^3) at room temperature because the temperature dependence of ρ is negligibly small as against the temperature dependence of v.

We measured the elastic modulus using a phase-comparison type pulse-echo method. Figure 10 shows a diagram of the pulse-echo method. Transducer which is the electric-acoustic translation device is bonded on both ends of a sample perpendicular to the propagation direction of ultrasound. If a pulse voltage is impressed to one transducer, ultrasound occurs from the transducer. The generated ultrasound repeats reflection at both ends of a sample, then, a pulse-echo sequence is outputted from other transducer. A propagation velocity v is given by following relation:

$$v = \frac{2l}{T} \tag{3.2}$$

where l is a distance between two transducer, that is a sample length, and T is a time interval of pulse-echo.

A block diagram of the phase-comparison method is shown in Fig. 11. The carrier wave of frequency f outputted from the oscillator is divided into a sample and reference side. The signal of sample side is formed into a drive pulse by a diode switch. The drive pulse is changed into the ultrasound by the transducer. Since the generated ultrasound repeats reflection at both ends of a sample, the phase of ultrasound delays in proportion to propagation time in a sample. The n-th pulse-echo is propagated in a sample for distance of $l(2n-1)$, that is time of $(2n-1)l/v$. Thus, a phase contrast $\Delta\phi_n$ between the phase of pulse-echo and reference signal is given by following equation:

$$\Delta\phi_n = 2\pi f \frac{(2n-1)l}{v} . \tag{3.3}$$

$\Delta\phi_n$ is detected by the phase detector. When the ultrasonic velocity v in a sample changes Δv, $\Delta\phi_n$ also changes with temperature change of a sample. Frequency f is changed Δf so as to take 0 for $\Delta\phi_n$. This process is presented as

$$\Delta\phi_n = 2\pi f \frac{(2n-1)l}{v} = 2\pi(f+\Delta f)\frac{(2n-1)l}{v+\Delta v} . \tag{3.4}$$

Thus, a relative change of ultrasonic velocity, $\Delta v/v$, is given by following equation:

$$\frac{\Delta v}{v} = \frac{\Delta f}{f} . \tag{3.5}$$

By measuring a relative change of frequency, the relative change of ultrasonic velocity in a sample is measured. Here, a temperature change of sample length l is negligibly

small. A block diagram of the equipment for ultrasonic measurement is shown in Fig 12. The details of device development was described elsewhere [16].

3.2.2 Measurements

We used the transducer made from $LiNbO_3$ which is fundamental frequency of $\sim$ 9MHz. RTV rubber was used as a bond between sample and transducer. Measurements were performed by putting the sample rod, which is attached the angle rotation cell, to a Variable Temperature Insert (VTI) with a 16 T superconducting magnet. Temperature was downed to 4.2 K using liquid ^{4}He and then downed to about 2 K by pomping liquid ^{4}He with the Alcatel pump. Intelligent Temperature Controller (ITC4) was used for temperature control with a heater. Temperature of sample was measured by a Carbon Glass Resistor (CGR) thermometer with the AC resistance bridge (AVS-46). The thermometer was calibrated from 1.3 K to 300 K in a zero magnetic field and from 1.3 to 150 K in H = 2.5, 5, 10 and 14 T. We measured the temperature dependence of elastic modulus C_{66} from 3 to 30 K in H = 2.5, 5, 7.5, 10, 12 and 14 T parallel to [100], [001] and [110] by the phase-comparison type pulse-echo method.

3.3 X-ray diffraction experiments

When the monochrome X-ray of wavelength λ is radiated to a powder polycrystal sample, λ is given by the Bragg equation:

$$\lambda = 2d_{hkl} \sin\theta \tag{3.6}$$

where θ is a incident angle of X-ray to a sample, d is a interval of lattice plane and hkl is the Miller index. Then, a diffraction peak of X-ray is observed in the direction of 2θ for the incident direction of X-ray.

We carried out the X-ray diffraction measurement in the cryogenic center of Hiroshima university. The intensity of X-ray diffraction was detected by the scintillation counter. Helium flow type cryostat which has the optical window for X-ray is connected with ^{4}He vessel by the transfer tube. The cryostat is cooled down by decompressed circulation of ^{4}He with a pump. Since a sample space, which is

sealed with the radiation shield, is changed into a vacuum state in advance and then a circulating decompressed state of ^{4}He, the sample space is maintained at nearly vacuum state. Temperature control was carried out by ITC4 with a heater. Powder polycrystal sample was taken on a Cu plate and fixed by Apiezon-N-grease which was melted and diluted with toluene. X-ray diffraction was measured as a function of $2\theta/\theta$ from 20 to 76° with a step width of 0.012° and a counting time of 2 s at 4.2, 10, 12, 20, 77, 296 K. Figure 13 shows a calculation result of diffraction peak position and intensity for UCu_2Sn by the Rietveld analysis. Numerical characters in parenthesis show the Miller index.

3.4 Thermal expansion measurements

3.4.1 Capacitance method

A capacitance method, which measures a change of capacitance between two electrodes as minute expansion and contraction of a sample, is one of techniques for thermal expansion measurement. Figure 14 shows a diagram of capacitance method. Sample is located between the inside of capacitance cell and the movable plate electrode. The movable plate electrode moves smoothly parallel to the fixed plate electrode in response to minute change of a sample length.

When only sample temperature is changed, minute change of parallel plate electrodes interval, that is minute change of the sample length, is detected as the change of capacitance. The capacitance C between parallel plate electrodes in Fig. 14 is given by the following equation:

$$C = \varepsilon_{\mathrm{d}} \frac{S}{d} \tag{3.7}$$

where S is a area of parallel plate electrodes, d is the parallel plate electrodes interval and ε_{d} is the dielectric constant between parallel plate electrodes. If minute change of capacitance, ΔC, varies in response to minute change of d, Δd, Δd is represented as

$$\frac{\Delta d}{d} = -\frac{\Delta C}{C} \quad . \tag{3.8}$$

Here, minute change of the sample length, Δl, is equal to $-\Delta d$. If $\Delta l = -\Delta d$ is substituted to formula 3.8, a thermal expansion $\Delta l/l$ is given by the following equation:

$$\frac{\Delta l}{l} = \frac{d}{l}\frac{\Delta C}{C} . \tag{3.9}$$

The resolution of our experiments, which is $d = 0.1$ mm, $C \simeq 12$pF, $\Delta C = 5 \times 10^{-6}$, is $\sim 10^{-8}$ for our ~ 3 mm sample.

So far, only a change of the sample length by temperature change is considered. However, it is difficult to measure only a change of the sample length by temperature change in actual measurement because the capacitance cell itself expands and contracts depending on temperature change. A change of the sample length by temperature change is obtained by subtracting a change of the capacitance cell from a measured total change when temperature of the capacitance cell keeps sample temperature. The parallel plate electrodes interval d increases in case that a sample is shrunk. Meanwhile, d decreases if the capacitance cell is shrunk. A change of parallel plate electrodes interval, $(\Delta d)^{\text{sample}}_{\text{meas.}}$, is given by following relation:

$$(\Delta d)^{\text{sample}}_{\text{meas.}} = -(\Delta l)^{\text{sample}} + (\Delta l)_{\text{cell}} \tag{3.10}$$

where $(\Delta l)^{\text{sample}}$ is a change of the sample length and $(\Delta l)_{\text{cell}}$ is a change of the capacitance cell. Temperature change of the capacitance cell is obtained to measure a standard sample that the thermal expansion is exactly decided. We measured the thermal expansion of copper as the standard sample [17]. Temperature change of capacitance cell is given by following relation:

$$(\Delta l)_{\text{cell}} = (\Delta d)^{\text{Cu}}_{\text{meas.}} + (\Delta l)^{\text{Cu}}_{\text{lit.}} \tag{3.11}$$

where $(\Delta l)^{\text{sample}}$ is equal to $(\Delta l)^{\text{Cu}}_{\text{lit.}}$ in case of copper as the standard sample. Thus, temperature change of the sample length is decided by following relation, using formulas 3.10 and 3.11:

$$(\Delta l)^{\text{sample}} = -(\Delta d)^{\text{sample}}_{\text{meas.}} + (\Delta d)^{\text{Cu}}_{\text{meas.}} + (\Delta l)^{\text{Cu}}_{\text{lit.}} . \tag{3.12}$$

3.4.2 Three-terminal method

The capacitance between parallel plate electrodes is exactly decided in case that these are covered by earthed conductor. Figures 15 and 16 show a diagram of the three-terminal method and a equivalent circuit of the three-terminal method, respectively. The capacitance between parallel plate electrodes, C_{X}, and a capacitance between parallel plate electrodes and earthed conductor, C_{HG} and C_{LG}, are called as the direct capacitance and the terminal capacitance, respectively. Figure 17 shows a diagram of bridge circuit to remove the terminal capacitance, where C_{S} is a standard capacitance, C_{HG}, C'_{HG}, C_{LG} and C'_{LG} are terminal capacitance and G is the earth. Only direct capacitance is detected as C_{X} by well balanced V_{X} with V_{S}. The bridge circuit is balanced without current flow in the detector D by adjusting the ratio of V_{X} and V_{S}. Then, a difference of voltages between G and E becomes zero and all current which flowed on C_{X} flow into C_{S}. Thus, a balance condition is given by following relation:

$$V_{\mathrm{S}}\, Y_{\mathrm{S}} = V_{\mathrm{X}}\, Y_{\mathrm{X}} \tag{3.13}$$

where Y_{X} and Y_{S} are the admittance of measured capacitance and standard capacitance, respectively.

In actual measurements, a parallel constituent impedance R^{P} caused by dielectric loss and insulating resistance and a serial constituent impedance R^{S} caused by contact resistance and resistance of lead wire exist in addition to the admittance. A influence of R^{P} rather than a influence of R^{S} is important in low frequency. The admittance Y is given by following equation:

$$Y = \frac{1}{R^{\mathrm{S}} + \frac{1}{j\omega C}} + \frac{1}{R^{\mathrm{P}}} \,. \tag{3.14}$$

Here, $\omega C R^{\mathrm{S}}$ is much less than 1 because of $f = 1$ kHz, $R^{\mathrm{S}} \sim 1\Omega$, $C = 12$ pF. The admittance Y is expanded as follows:

$$Y \sim j\omega C \left[1 - \left(\omega C R^{\mathrm{S}} + \frac{1}{\omega C R^{\mathrm{P}}}\right)\right] \,. \tag{3.15}$$

R^{S} is negligible because of $R^{\mathrm{P}} \sim 10^7$, that is $\omega C R^{\mathrm{P}} \sim 1$. Therefore, formula 3.15 is represented as

$$Y = j\omega C + \frac{1}{R^{\mathrm{P}}} \,. \tag{3.16}$$

It assumes that R^{P} component and admittance corresponding to the capacitance C_{X}, C_{S} are R_{X}, R_{S} and Y_{X}, Y_{S}, respectively. Formula 3.16 is rewrote as follows:

$$Y_{\mathrm{S}} = j\omega C_{\mathrm{S}} + \frac{1}{R_{\mathrm{S}}} \tag{3.17}$$

$$Y_{\mathrm{X}} = j\omega C_{\mathrm{X}} + \frac{1}{R_{\mathrm{X}}} . \tag{3.18}$$

Using formulas 3.13, 3.17 and 3.18, the balance condition is given by following equation:

$$V_{\mathrm{S}}\left(j\omega C_{\mathrm{S}} + \frac{1}{R_{\mathrm{S}}}\right) = V_{\mathrm{X}}\left(j\omega C_{\mathrm{X}} + \frac{1}{R_{\mathrm{X}}}\right) . \tag{3.19}$$

If formula 3.19 is divided into a real part and an imaginary part, formula 3.19 is rewrote as follows:

$$C_{\mathrm{X}} = C_{\mathrm{S}}\frac{V_{\mathrm{S}}}{V_{\mathrm{X}}} \tag{3.20}$$

$$R_{\mathrm{X}} = R_{\mathrm{S}}\frac{V_{\mathrm{X}}}{V_{\mathrm{S}}} . \tag{3.21}$$

Thus, if a real part and an imaginary part are balanced independently, capacitance C_{X} can be measured exactly.

3.4.3 Measurements

We have manufactured the capacitance cell based on the three-terminal capacitance method [18]. Figure 18 shows the structure of our capacitance cell. Our capacitance cell becomes uniform temperature quickly without local distortion in response to a temperature change since components of capacitance cell, which are made from copper, are wholly column-shaped. Both plane of the plate electrode was polished so as to be parallel. The movable plate electrode always moves in parallel to the fixed plate electrode because the movable plate electrode is supported by three rods and a sample is fixed with spring. We used a flexible Be-Cu spring in fear of the influence of tension from a spring to a sample as possible. Since a sample space is fixation, we needed to prepare one spacer about one axis. It is a possibility that the present experimental setup may disregard the ε_{xy} strain technically even though it emerges. As depicted in Fig.19(a), a change in the sample length along

the x direction, consequently the strain $\varepsilon_{xx} - \varepsilon_{yy}$, can be directly measured since we capacitively detect the change in spacing between the parallel plate electrodes. In the case of the strain ε_{xy}, the sample will rotate so as to fit the two surfaces of the sample onto the parallel plates as shown in Fig.19(b). The change Δd in the parallel plate electrodes interval will be negligibly small because Δd is proportional to $(1 - \frac{3}{2}\varepsilon_{xy}^2 + \cdots)$. Temperature of sample was measured by a cernox thermometer, which was calibrated from 1.5 K to 280 K, with the AC resistance bridge (AVS-47). The thermometer thermally contacts with the capacitance cell by Apiezon-N-grease. To avoid a earth loop, only one coaxial cable, which is made from stainless to prevent a heat influx from outside, was earthed. Thermal expansion was measured as a function of temperature T from 4.2 to 40 K with a temperature interval of 0.1 K along the a, b and c axes using the capacitance bridge (ANDEEN HAGERING 2500A). The b axis is defined as perpendicular to the a axis in the hexagonal c plane. The value of $\Delta l/l$ for each axis was defined as ($l(T) - l(40\mathrm{K})$) / $l(40\mathrm{K})$.

Chapter 4

Results & Discussion

4.1 CEF parameters

4.1.1 Elastic modulus C_{66} in magnetic field

Figures 20, 21 and 22 show the temperature dependence of C_{66} in the magnetic field parallel to [100], [001] and [110], respectively. We made out the $H-T$ phase diagram of UCu_2Sn shown in Fig. 23, assuming that T_Q is the minimum point of data. In H // [100], a softening of elastic modulus at T_Q is strongly suppressed with increasing H. T_Q shows a bending in low magnetic field and then decreases monotonically with increasing H. The softening of elastic modulus at T_Q is suppressed gradually and T_Q decreases with increasing H in H // [001]. In H // [110], the softening of elastic modulus at T_Q is strongly suppressed and T_Q increases monotonically with increasing H.

4.1.2 Strain susceptibility

In our compound, a elastic strain induced by the ultrasound linearly couples to the quadrupole moment derived from $5f$ electrons and affects $5f$ electron state as a perturbation. The perturbation Hamiltonian H_{ME} is given by following equation:

$$H_{\mathrm{ME}} = \sum_i g_{\Gamma_i} O_i \varepsilon_i \ . \tag{4.1}$$

The calculation of strain susceptibility is performed by the Wigner-Brillouin perturbation method. When the elastic strain is induced, each energy eigenvalue divided

by CEF, which is took a perturbation to the second-order into consideration, is presented as

$$E_i(\varepsilon_\Gamma) = E_i^0 + g_\Gamma \langle i|O_\Gamma|i\rangle \varepsilon_\Gamma + g_\Gamma^2 \sum_{i\neq j} \frac{|\langle i|O_\Gamma|j\rangle|^2}{E_i^0 - E_j^0} \varepsilon_\Gamma^2 \tag{4.2}$$

where E_i^0 is an energy eigenvalue in non-perturbation state. A free energy of Helmholtz contributed from $5f$ electrons, $F_{\rm ion}$, is given by following equation:

$$\begin{aligned} F_{\rm ion}(\varepsilon_\Gamma, T) &= -{\rm N}_0 k_{\rm B} T \ln Z(\varepsilon_\Gamma, T) \\ &= -{\rm N}_0 k_{\rm B} T \ln \left[\sum_i \exp\left(-\frac{E_i(\varepsilon_\Gamma)}{k_{\rm B} T} \right) \right] \end{aligned} \tag{4.3}$$

where Z is the partition function and $k_{\rm B}$ is the Boltzmann constant. Meanwhile, a free energy originated from a kinetic energy and a potential energy of electrons other than 5f electrons, $F_{\rm lattice}$, is presented as

$$F_{\rm lattice} = \frac{1}{2} C_\Gamma^0 \varepsilon_\Gamma^2 \ . \tag{4.4}$$

The total free energy $F_{\rm total}$ is accordingly given by following equation:

$$F_{\rm total} = F_{\rm ion} + F_{\rm lattice} \ . \tag{4.5}$$

The elastic modulus $C_{\Gamma,{\rm ME}}$ is defined by the second-order differentiation of total free energy with respect to ε_Γ and given by following equation:

$$C_{\Gamma,{\rm ME}}(T) = \left(\frac{\partial^2 F_{\rm total}(\varepsilon_\Gamma, T)}{\partial \varepsilon_\Gamma^2} \right)_{\varepsilon_\Gamma \to 0} \equiv C_\Gamma^0 - {\rm N}_0 g_\Gamma^2 \chi_s^\Gamma(T) \tag{4.6}$$

where χ_s^Γ is the strain susceptibility. χ_s^Γ with E_i in formula 4.2 is presented as

$$-g_\Gamma^2 \chi_s^\Gamma(T) = -\sum_i \left[\left\langle -\frac{\partial^2 E_i}{\partial \varepsilon_\Gamma^2} \right\rangle + \frac{1}{k_{\rm B} T} \left\{ \left\langle \left(\frac{\partial E_i}{\partial \varepsilon_\Gamma} \right)^2 \right\rangle - \left\langle \frac{\partial E_i}{\partial \varepsilon_\Gamma} \right\rangle^2 \right\} \right] \tag{4.7}$$

where $\langle\ \rangle$ denotes a heat statistics average of the Boltzmann distribution. First and second term in formula 4.7 are called as Van-Vleck and Curie term, respectively, as is the case with the magnetic susceptibility. Van-Vleck and Curie term are contributed from off-diagonal and diagonal element of the quadrupole operator, respectively.

In addition to the interaction of strain-quadrupole coupling, the interaction of q-q coupling also occurs. The Hamiltonian originated from q-q coupling, $H_{\mathrm{Q-Q}}$, using the molecular field approximation, is given by following equation:

$$H_{\mathrm{Q-Q}} = -g'_{\Gamma_i} \sum_{\Gamma_i} \sum_{j} \langle O_{\Gamma_i} \rangle O_{\Gamma_i}(j) \ . \tag{4.8}$$

Thus, The temperature dependence of elastic modulus $C_\Gamma(T)$ is given by the following equation:

$$C_\Gamma(T) = \frac{-\mathrm{N}_0 g_\Gamma^2 \chi_\Gamma(T)}{1 - g'_{\Gamma_i} \chi_\Gamma(T)} + C_0 \tag{4.9}$$

where C_0 is the linear T dependence of the back ground stiffness assumed as

$$C_0 = a + bT \ . \tag{4.10}$$

4.1.3 CEF parameters

We consider an effective Hamiltonian H_{eff} in zero magnetic field;

$$\begin{aligned}
H_{\mathrm{eff}} &= H_{\mathrm{CEF}} - H_{\mathrm{ME}} + H_{\mathrm{Q-Q}} & (4.11)\\
H_{\mathrm{CEF}} &= B_2^0 O_2^0 + B_4^0 O_4^0 + B_6^0 O_6^0 + B_6^6 O_6^6 & (4.12)\\
H_{\mathrm{ME}} &= g_{\Gamma_5}(O_{xy}\varepsilon_{xy} + O_2^2 \varepsilon_t) + g_{\Gamma_6}(O_{yz}\varepsilon_{yz} + O_{zx}\varepsilon_{zx}) \\
&\quad + g_{\Gamma_1^{\mathrm{u}}} O_2^0 \varepsilon_{\Gamma_1^{\mathrm{u}}} + (g^{\alpha}_{\Gamma_1^{\mathrm{B}}} O_2^0 + g^{\beta}_{\Gamma_1^{\mathrm{B}}} O_4^0 + g^{\gamma}_{\Gamma_1^{\mathrm{B}}} O_6^0 + g^{\delta}_{\Gamma_1^{\mathrm{B}}} O_6^6)\varepsilon_{\Gamma_1^{\mathrm{B}}} & (4.13)\\
H_{\mathrm{Q-Q}} &= -g'_{\Gamma_i} \langle O_{\Gamma_i} \rangle O_{\Gamma_i} & (4.14)
\end{aligned}$$

where B_m^n is CEF parameter. In a magnetic field, the Zeeman term:

$$H_{Zeeman} = -g_J \mu_B J \cdot H \tag{4.15}$$

is added to the formula 4.11.

We have optimized the CEF parameters in order to reproduce the data of entropy, magnetic susceptibility, elastic moduli and C_{66} in the magnetic field. Figures 24, 25 and 26 show the fitting result of C_{66} in case of $H = 5, 14$ T along [100], [001] and [110], respectively. Theoretical curves by solid line good reproduce all data with the parameters listed in Tables 1 and 2. Figure 27 shows the fitting result of

magnetic susceptibility in case of a and b axes. Theoretical curves good reproduce all data above T_Q with CEF. The data below T_Q is reproduced by 60 degree domain structure. Theoretical curve assumed for 60 degree domain structure is smaller than the data above T_Q because of equally probability 60 degree domain structure. The calculated entropy by CEF parameters is shown in Fig. 28. The data of entropy is almost reproduced by CEF parameters though a little deviance is seen between the data and theoretical curve. The CEF level scheme corresponding to CEF parameters in Table 1 is shown in Fig. 29. The analysis of data proposed the level scheme in which the first excited state Γ_4 is situated at 109 K, the second excited state Γ_6 at 332 K and $\cdots$ above the ground state doublet Γ_5. Figure 30 shows the $H-T$ phase diagram of UCu_2Sn, assuming that T_Q is the minimum point of the data and theoretical curve. Theoretical curves well reproduce $H-T$ phase diagram in all H // [100], [001] and [110]. T_Q increases monotonically with increasing H // [110]. It is estimated that quadrupole moment is strongly induced because of a mixing between the ground state and exited state in H // [110].

4.2 X-ray diffraction

Figure 31 shows a X-ray diffraction peak of UCu_2Sn at 20 K and 4.2 K, that is above and below T_Q. Experimental results show almost same diffraction peak as the calculation result in Rietveld analysis shown in Fig. 13. Diffraction peak at 43.3, 50.5 and 74.3° in experimental results are caused by Cu which is a basal plate of the sample. The difference was not found in the position of diffraction peak between above and below T_Q. Therefore, we did not succeed in detecting any indication for the spontaneous occurrence of macroscopic strain.

We numerically calculated the magnitude of strain taking account of the strain-quadrupole coupling constant of Γ_5, g_{Γ_5}, in the analysis of elastic modulus by using the relation [19]

$$|\varepsilon_{\Gamma_5}| = \frac{N_0 k_B g_{\Gamma_5} \langle O_{\Gamma_5} \rangle}{C_0} \tag{4.16}$$

where $|g_{\Gamma_5}| = 9.3$ K, $C_0 \simeq 34$, $\langle O_{\Gamma_5} \rangle \simeq 5$ at 0 K and $k_B = 1.38 \times 10^{-23}$ (J/K). The evaluated value ($\simeq 2.50 \times 10^{-4}$) was smaller than the experimental resolution

($\simeq 1 \times 10^{-3}$).

4.3 Thermal expansion

Figure 32 shows temperature dependence of thermal expansion $\Delta l/l$ both for along the a and b axes. At high temperatures, both of $\Delta l/l$ along the a and b axes decrease monotonically with decreasing temperature. At low temperatures below $T_{\rm Q}$, $\Delta l/l$ along the a axis, that is $\Delta a/a$, rapidly increases with decreasing temperature, whereas $\Delta l/l$ along the b axis, that is $\Delta b/b$, continues to decrease. As far as the crystal keeps a hexagonal symmetry, $\Delta a/a$ and $\Delta b/b$ should coincide with each other even though it thermally expands or contracts. But results of $\Delta a/a$ and $\Delta b/b$ differ with each other below $T_{\rm Q}$. As clearly seen in Fig. 32, $\Delta a/a$ starts to deviate from $\Delta b/b$ at $\sim$ 20 K. This behavior appears to correspond closely to that of the transverse modulus C_{66} which starts to soften gradually below $\sim$ 20 K. The precursor is possibly ascribed to the fluctuation of the quadrupolar ordering. Figure 33 shows the difference $\Delta a/a - \Delta b/b$, which is proportional to the expected spontaneous strain $\varepsilon_{xx} - \varepsilon_{yy}$. The $\varepsilon_{xx} - \varepsilon_{yy}$ strain is one of the ε_{Γ_5} strains. Thus, we succeeded in direct confirmation of the macroscopic distortion due to the ferroquadrupolar ordering in UCu_2Sn. The ground state doublet Γ_5 has a degeneracy of quadrupoles O_{xy} and O_2^2. One of these order parameters should emerge below $T_{\rm Q}$ and therefore the corresponding strain of ε_{xy} or $\varepsilon_{xx} - \varepsilon_{yy}$ is expected to appear spontaneously. In the present experiment, only the $\varepsilon_{xx} - \varepsilon_{yy}$ component which linearly couples to O_2^2 was detected. This result strongly suggests that the order parameter is O_2^2. The magnitude of the strain evaluated at 5 K is $\sim 4.5 \times 10^{-5}$. This is the reason why we could not detect any corresponding strain by the powder X-ray diffraction with a resolution of 10^{-3}. However, the present value is one order of magnitude smaller than the value of 2.5×10^{-4} which was estimated from the parameter values fitted to the elastic modulus observed. When a hexagonal system undergoes a structural transition, a 60 degrees ferroelastic-type domain is expected to appear in the ordered state. In the present case of UCu_2Sn, we believe to have observed the average of the spontaneous strain over those domains. The calculated value of 2.5×10^{-4} should be regarded as the maximum value of the macroscopic strain expected for a

single-domain sample.

Shown in Fig. 34 is the temperature dependence of thermal expansion $\Delta l/l$ along the c axis, that is $\Delta c/c$. At high temperatures, $\Delta c/c$ decreases monotonically with decreasing temperature. It increases gradually below $\sim$ 20 K and rapidly below $T_{\rm Q}$. The magnitude of the strain evaluated at 5 K is $\sim 2.0 \times 10^{-5}$. This behavior is difficult to explain by only quadrupolar ordering of Γ_5 since a change caused by Γ_5 strain is large within xy-plane. $\Delta c/c$ calculated by CEF was unreproducible for a increase of $\Delta c/c$ below $T_{\rm Q}$. We have no convincing explanation for this increase in $\Delta c/c$, but a possible origin might be related to development of the secondary order parameter O_2^0 which couples to $2\varepsilon_{zz} - \varepsilon_{xx} - \varepsilon_{yy}$. The strain-quadrupole coupling constant between $2\varepsilon_{zz} - \varepsilon_{xx} - \varepsilon_{yy}$ and O_2^0 is very large shown in Table 2.

The thermal expansion coefficient α_i is related to $\delta l/l$ by the following equation:

$$\alpha_i = \frac{1}{\delta T}\frac{\delta l_i}{l_i},$$

where δ and the subscript i denote an infinitesimal deference and each axis, respectively. Figure 35 shows the thermal expansion coefficients α as a function of temperature along the a, b and c axes. Here, we assumed that the background variation of the thermal expansion coefficient is given by $\alpha_{\rm bg} = AT + BT^3$ [20]. The values used for the fitting parameters A and B are listed in Table 3. From these data, we can estimate the pressure effects on the transition temperature $T_{\rm Q}$, using the Ehrenfest relation:

$$\frac{{\rm d}T_{\rm Q}}{{\rm d}P} = \frac{\Delta\beta T_{\rm Q} V_{\rm m}}{\Delta C_{\rm p}},$$

where the volume expansion coefficient $\Delta\beta$ is assumed as $\Delta\beta = \Delta\alpha_a + \Delta\alpha_b + \Delta\alpha_c$. $V_{\rm m}$ is the molar volume and $\Delta C_{\rm p}$ is the change in the isobaric specific heat at $T_{\rm Q}$. We used the difference between $\alpha_{\rm bg}$ and α_i for $\Delta\alpha_i$ at $T_{\rm Q}$. The uniaxial pressure effects on the transition temperature $T_{\rm Q}$ are estimated from this result. The values of ${\rm d}T_{\rm Q}/{\rm d}P_i$ along the a, b and c axes are listed in Table 4. We can estimate the uniaxial pressure dependence of transition temperature in UCu_2Sn for the first time. The hydrostatic pressure effect on $T_{\rm Q}$ is also estimated to be ${\rm d}T_{\rm Q}/{\rm d}P = -6.0 \times 10^{-1}$ K/GPa. This value is quite consistent with the value ${\rm d}T_{\rm Q}/{\rm d}P = -9.6 \times 10^{-1}$ K/GPa reported for polycrystalline UCu_2Sn in the hydrostatic pressure by Kurisu *et al.* [21].

The quantum critical point, that ferroquadrupolar ordering disappears, will be seen about 26 GPa. The diamond anvil cell which generates high pressure is required to attain the quantum critical point in UCu_2Sn.

4.4 Pressure cell for ultrasonic measurements

To search a influence of pressure to the quadrupolar ordering, we are developing the pressure cell which is possible to measure the elastic modulus with the ultrasound. A diagram of the pressure cell for ultrasonic measurement is shown in Fig. 36. The Co-Ni alloy (MP35N) which is high intensity and non-magnetic was used for the pressure cell [22]. The diameter of a sample space is 5 mm. The sample space which is filled by a pressure medium is pressurized by hand-operated press machine and retained pressure by closing a clamping bolt. We used a fluorinert as the pressure medium. The pressure in low temperature is checked at the superconductivity transition temperature of Pb. The pressure, which is put at room temperature, decreases with decreasing temperature, since a percentage of heat contraction of the pressure cell differs from that of the fluorinert. The pressure in the pressure cell at low temperature, $P_{\mathrm{L.T.}}$, is estimated by following equation [23]:

$$T_{\mathrm{c}}(P) = T_{\mathrm{c}}(0) - 0.365 P_{\mathrm{L.T.}} \ .$$

Figure 37 shows a diagram of the electrical feedthrough and sample space. A co-axial cable, which transmits a signal without the influence of electromagnetic wave from the surrounding, is needed for ultrasonic measurement. However, the fluorinert escapes from the co-axial cable at the time of pressurization in case of the co-axial cable is put into the sample space. At the beginning, co-axial cables were changed into Cu wires at a outside of electrical feedthrough. In this case, measurement was difficult due to the noise from a coupling of high frequency and so on. Therefore, co-axial cables were put into the position hardened with the stycast near the sample space. Though the stycast became weak to inner pressure, the noise of a signal decreased sharply. Core wires and shield wires of co-axial cables are changed into Cu wires within stycast. Signal and ground side of transducer made from $LiNbO_3$ are contacted to Cu wires with In solder. Since $LiNbO_3$ is a ferroelectric, signal

and ground side of transducer are needed to earth at the time of pressurization. Figure 38 shows a pulse-echo of quartz pressurized by 1 GPa at room temperature. The pulse-echo which is a little noise is measurable.

Chapter 5

Conclusion

We measured the elastic modulus C_{66} in the magnetic field parallel to [100], [001] and [110] by the phase-comparison type pulse-echo method and made out the $H-T$ phase diagram of UCu_2Sn. So, we optimized the CEF parameters so as to reproduce the data of entropy, magnetic susceptibility, elastic moduli and C_{66} in the magnetic field parallel to [100], [001] and [110]. The proposed level scheme is the ground state doublet Γ_5, the first excited state Γ_4 at 109 K and $\cdots$. The $H-T$ phase diagram is well reproduced. To confirm the ferroquadrupolar ordering in UCu_2Sn which is indicated from the fitting of elastic modulus, we manufactured the capacitance cell and measured the thermal expansion of single-crystalline UCu_2Sn along the a, b and c axes. The change in the thermal expansion below T_Q clearly indicates the spontaneous emergence of the macroscopic strain $\varepsilon_{xx} - \varepsilon_{yy}$, which couples to the quadrupole O_2^2. As a result, it is completely proved that the transition in UCu_2Sn at T_Q originates from the ferroquadrupolar ordering. The enhancement of $\Delta c/c$ below T_Q might be regarded as due to the development of the secondary order parameter O_2^0. We also discussed the uniaxial pressure effect on T_Q, and succeeded in evaluating $\mathrm{d}T_Q/\mathrm{d}P_i$ for the first time.

Acknowledgement

The author is grateful to Professor Takashi Suzuki for giving him valuable advice, stimulating discussion and continuous encouragement through the course of this work. He also wishes to express his sincere thanks to Professor Akira Tamaki, Susumu Hashio, Professor Toshizo Fujita, Associate Professor Ryuta Yagi, Doctor Fumihiko Nakamura and Doctor Masakazu Ito for numerous discussion and useful advice. He wishs to express his appreciation to Professor Toshiro Takabatake and Doctor Kenichi Kato for the preparation of UCu_2Sn crystal. He is grateful to Doctor Noriki Okuda, Haruhiro Higaki and Hiroshi Goshima for technical advice and support of experiment, to Suzuki laboratory members for generous collaboration. He thanks the Cryogenic Center of Hiroshima University for their experimental backup. This work was supported by Grant-in-Aids for both Scientific Research (B) (No.13440114) and COE Research (No.13CE2002) from the Ministry of Education, Culture, Sports, Science and Technology of Japan.

References

[1] P.Morin, D.Schmitt :in Ferromagnetic Materials, vol.5 (North-Holland, Amsterdam 1990) ed. K.H.J.Buschow and E.P.Wohlfarth, p.1.

[2] P.Santini and G.Amoretti Phys. Rev. Lett. **85**, 2188 (2000).

[3] K.A.McEwen, U.Steigenberger, K.N.Clausen, J.Kulda, J.G.Park, and M.B.Walker J. Magn. Magn. Mater. **177-181**, 37 (1998).

[4] P.Santini and G.Amoretti Phys. Rev. Lett. **73**, 1027 (1994).

[5] T.Akazawa, T.Suzuki, H.Goshima, T.Tahara, T.Fujita, T.Takabatake and H.Fujii J. Phys. Soc. Jpn. **67**, 3256 (1998).

[6] T.Suzuki, I.Ishii, N.Okuda, K.Katoh T.Takabatake, T.Fujita and A.Tamaki Phys. Rev. B **62**, 49 (2000).

[7] T.Kasuya BUTSURI, The Physical Society of Japan **42**, 725 (1987).

[8] H.Iwasaki :M.Thesis, Hiroshima university (1992)

[9] H.H.Hill :Plutonium and Other Actinides (AIME, New York, 1970) ed. W.M.Miner, p.2.

[10] T.Takabatake, H.Iwasaki, H.Fujii, S.Ikeda S.Nishigori, Y.Aoki, T.Suzuki and T.Fujita J. Phys. Soc. Jpn. **61**, 778 (1992).

[11] T.Takabatake, M.Shirase, K.Katoh, Y.Echizen, K.Sugiyama and T.Osakabe J. Magn. Magn. Mater. **177-181**, 53 (1998).

[12] S.Wiese, E.Gamper, H.Winkelmann, B.Büchner, M.M.Abd-Elmeguid, H.Micklitz, T.Takabatake Physica B **230-232**, 95 (1997).

[13] K.Kojima, A.Harada, T.Takabatake, S.Ogura, K.Hiraoka, Physica B **269**, 249 (1999).

[14] W.Higemoto, A.Koda, R.Kadono, Y.Echizen, T.Takabatake Physica B **281** & **282**, 234 (2000).

[15] P.M.Levy, P.Morin, and D.Schmitt Phys. Rev. Lett. **42**, 1417 (1979).

[16] T.Suzuki :D.Thesis, Tohoku university (1987)

[17] F.R.Kroeger and C.A.Swenson Journal of Applied Physics **48**, 853 (1977).

[18] A.de Visser :Ph.D.Thesis, Amsterdam university (1986)

[19] B. Lüthi, in *Dynamical Properties of Solids* edited G. K. Horton and A. A. Maradudin (NorthHolland, Amsterdam 1980).

[20] T.H.K.Barron, J.G.Collons and G.K.White Advances Physics **29**, 609 (1980).

[21] M.Kurisu, T.Takabatake, H.Iwasaki and H.Fujii Physica B **206** & **207**, 505 (1995).

[22] I.R.Walker :Review of Scientific Instruments **70**, 3402 (1999).

[23] A Eilimg and J.S.Schilling J.Phys. F: Metal Phys., **11**, 623-39 (1981).

Table 1: CEF parameters of UCu_2Sn obtained from the fitting of entropy, magnetic susceptibility, elastic moduli and C_{66} in the magnetic field.

B_2^0 (K)	B_4^0 (K)	B_6^0 (K)	B_6^6 (K)
0.1083	-3.899×10^{-2}	-3.973×10^{-3}	0.1532

Table 2: Obtained parameters in the fitting of elastic moduli.
$|g_{\Gamma_i}|$ (K), g'_{Γ_i} (K), a (GPa) and b ($\times 10^{-3}$ GPa/K)

Op.	O_{xy}	O_{yz}	O_2^0	O_4^0	O_6^0	O_6^6
$\|g_{\Gamma_i}\|$	9.32	130.4	24.36^{u} 28.83^{B}	0.084	0.005	1.255
g'_{Γ_i}	0.496	-1.080	–	–	–	–
mode	C_{66} (Γ_5)	C_{44} (Γ_6)	C_{33} (Γ_1^{B}, Γ_1^{u})	C_{11} (Γ_1^{B} , Γ_1^{u} , Γ_5)		
a	33.85	40.04	62.25	80.70		
b	-5.000	-6.752	-11.99	-16.14		
D	1050	–	–	–		

Table 3: Fitting parameters A and B for the background α_{bg} of thermal expansion coefficients.

axis	A (K^{-2})	B (K^{-4})
a, b	3.21×10^{-8}	3.73×10^{-11}
c	6.46×10^{-8}	4.75×10^{-11}

Table 4: Uniaxial pressure effects on the transition temperature T_{Q}. The values for $\mathrm{d}T_{\mathrm{Q}}/\mathrm{d}P_i$ are listed in K/Pa.

$\mathrm{d}T_{\mathrm{Q}}/\mathrm{d}P_a$	$\mathrm{d}T_{\mathrm{Q}}/\mathrm{d}P_b$	$\mathrm{d}T_{\mathrm{Q}}/\mathrm{d}P_c$
-4.02×10^{-10}	$+2.65 \times 10^{-10}$	-4.60×10^{-10}

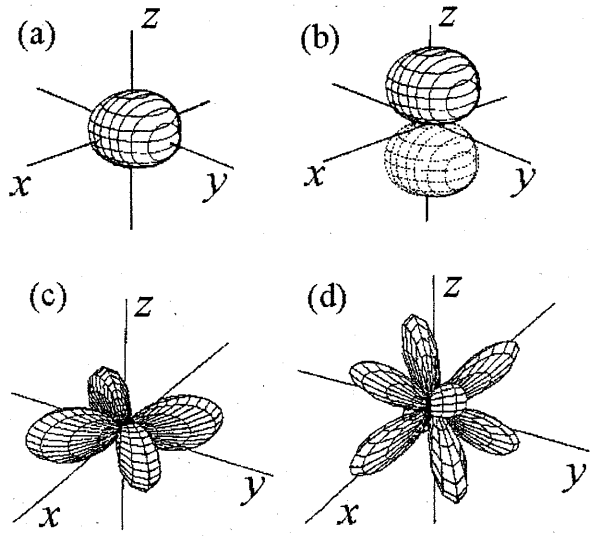

Figure 1: Wave function of (a) s orbit, (b) p orbit, (c) d orbit and (d) f orbit by way of example.

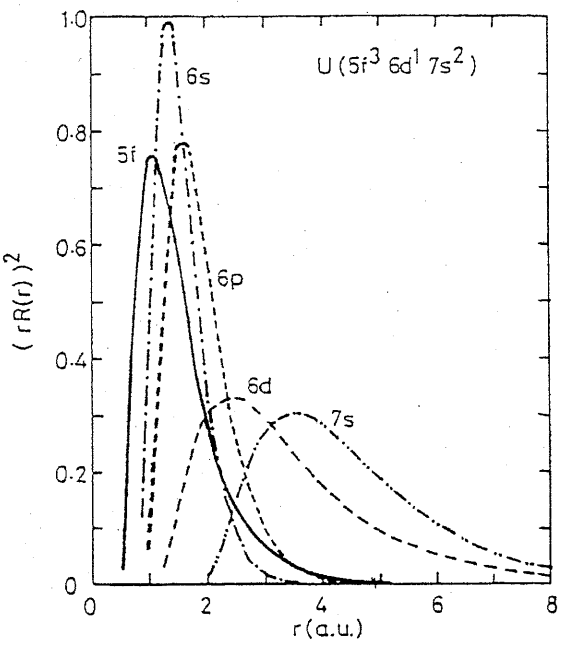

Figure 2: Wave function of U atom [7].

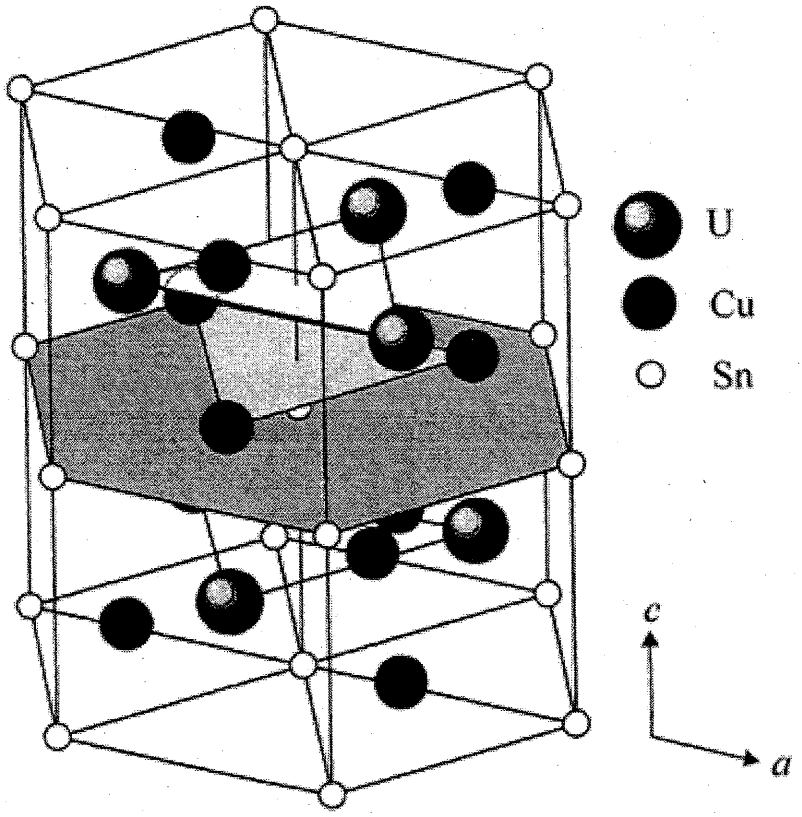

Figure 3: The crystal structure of UCu_2Sn.

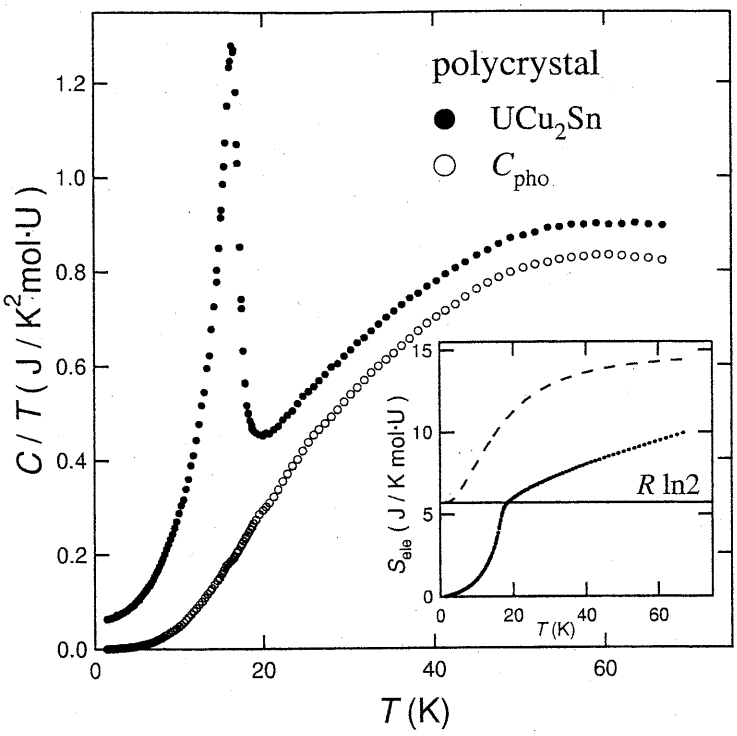

Figure 4: The specific heat of UCu_2Sn and its phonon contribution estimated from the specific heat of reference compound $ThCu_2Sn$ are shown by solid and open circles, respectively. The electronic entropy and calculated entropy using the CEF [6] are shown by solid circles and broken curve, respectively, in the inset.

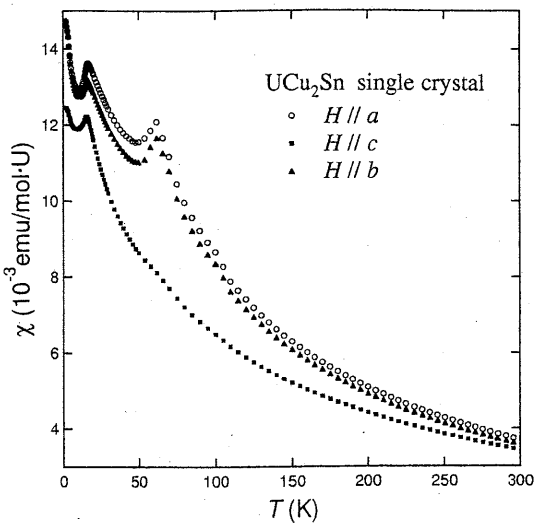

Figure 5: The magnetic susceptibility of UCu_2Sn along a, b and c axes are shown by open circles, solid triangles and solid squares, respectively.

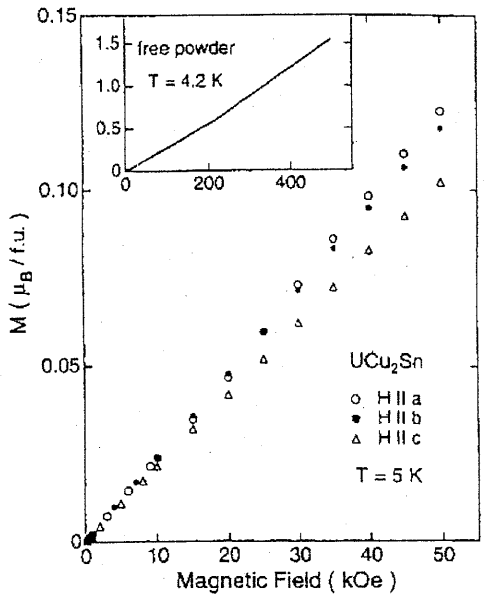

Figure 6: The magnetization curve of UCu_2Sn. The magnetization curve in upfield is shown in the inset [11].

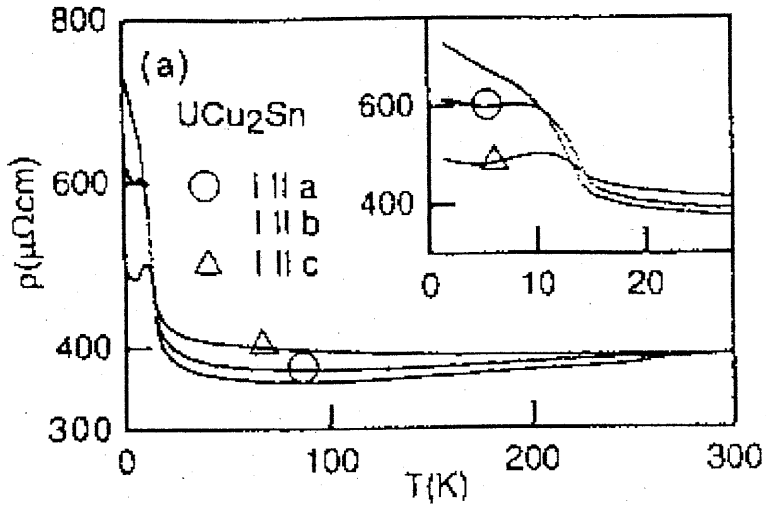

Figure 7: The electrical resistivity of UCu_2Sn [11].

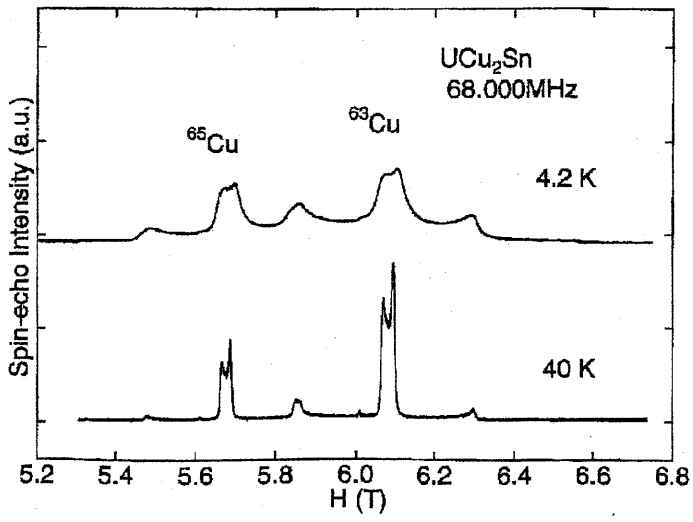

Figure 8: NMR spectroscopy of UCu_2Sn above and below T_Q [13].

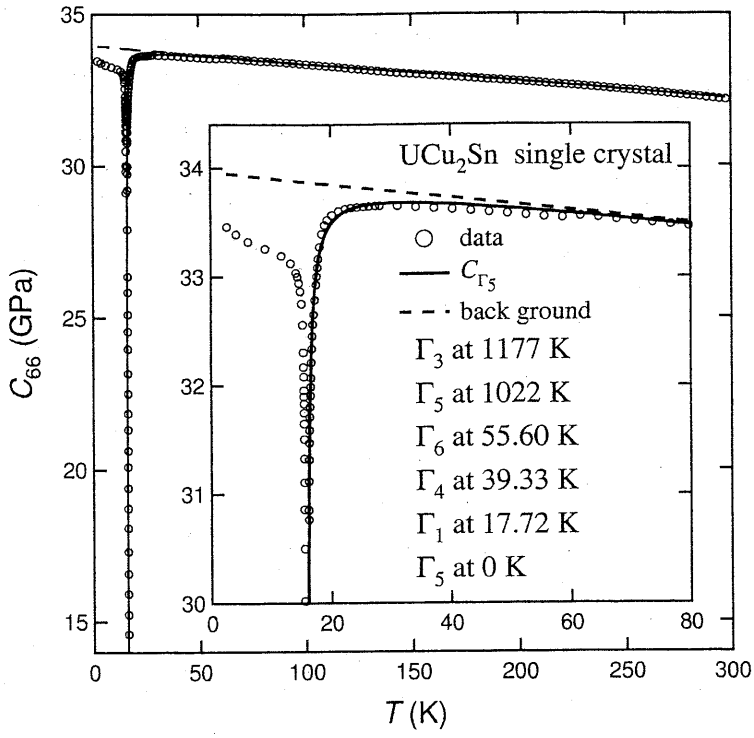

Figure 9: Temperature dependence of C_{66}. The solid curve and the broken line show the fitting of C_{Γ_5} and the back ground stiffness, respectively. The inset demonstrates the same data in an expanded scale.

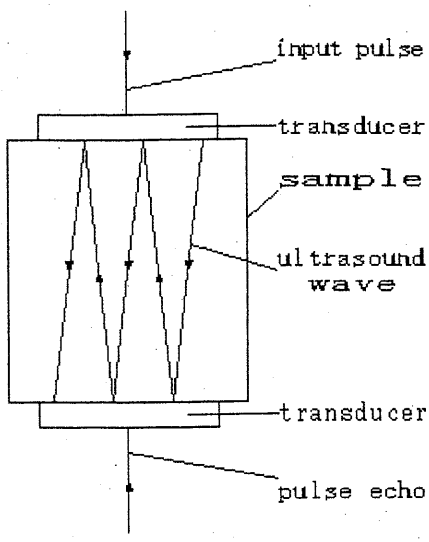

Figure 10: A diagram of the pulse-echo method.

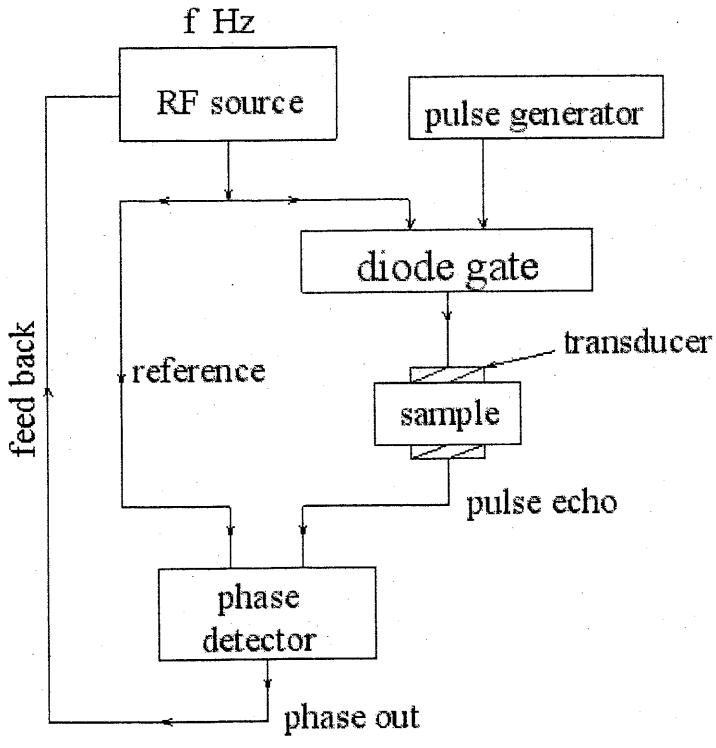

Figure 11: A block diagram of the phase-comparison method.

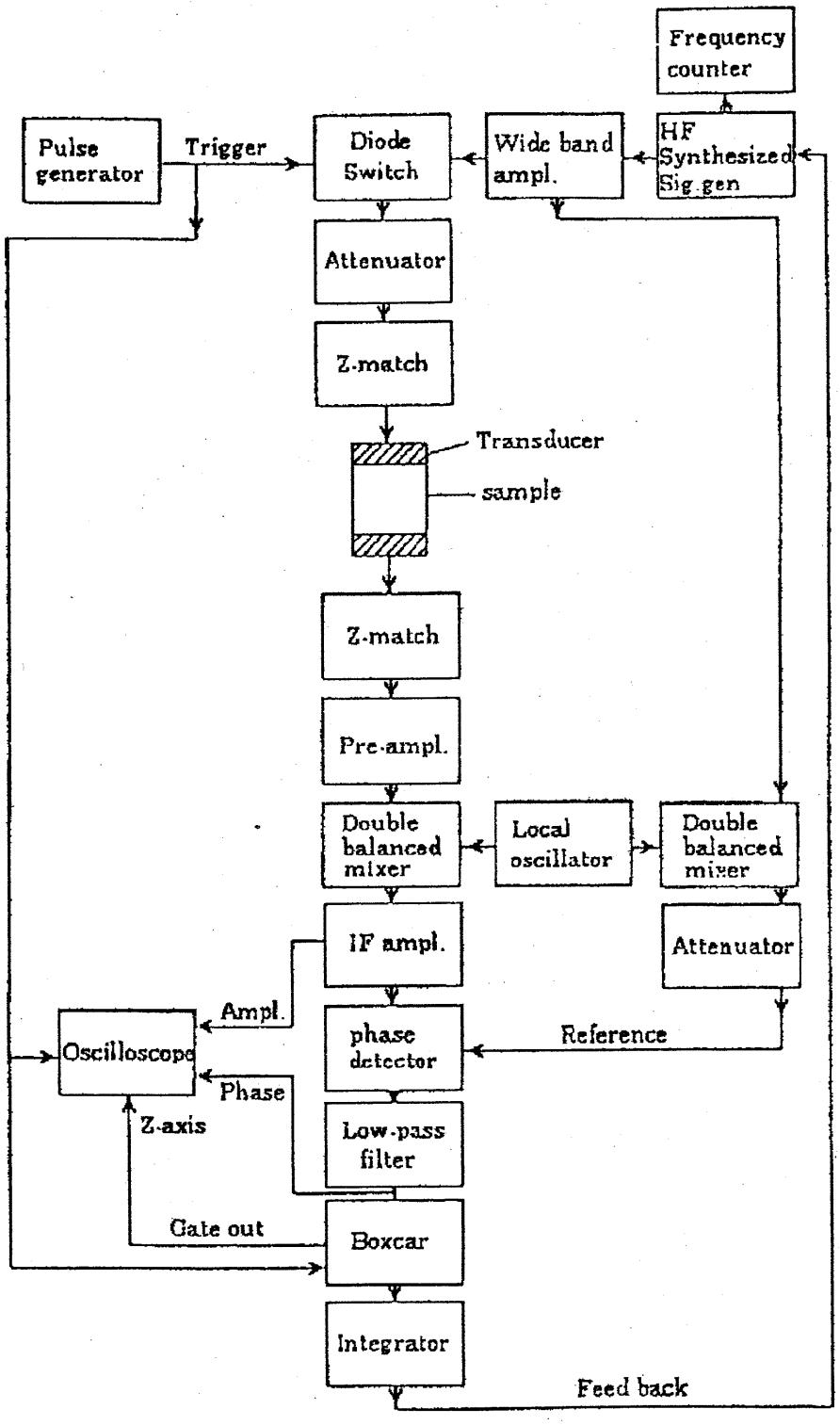

Figure 12: A block diagram of the equipment for ultrasonic measurement.

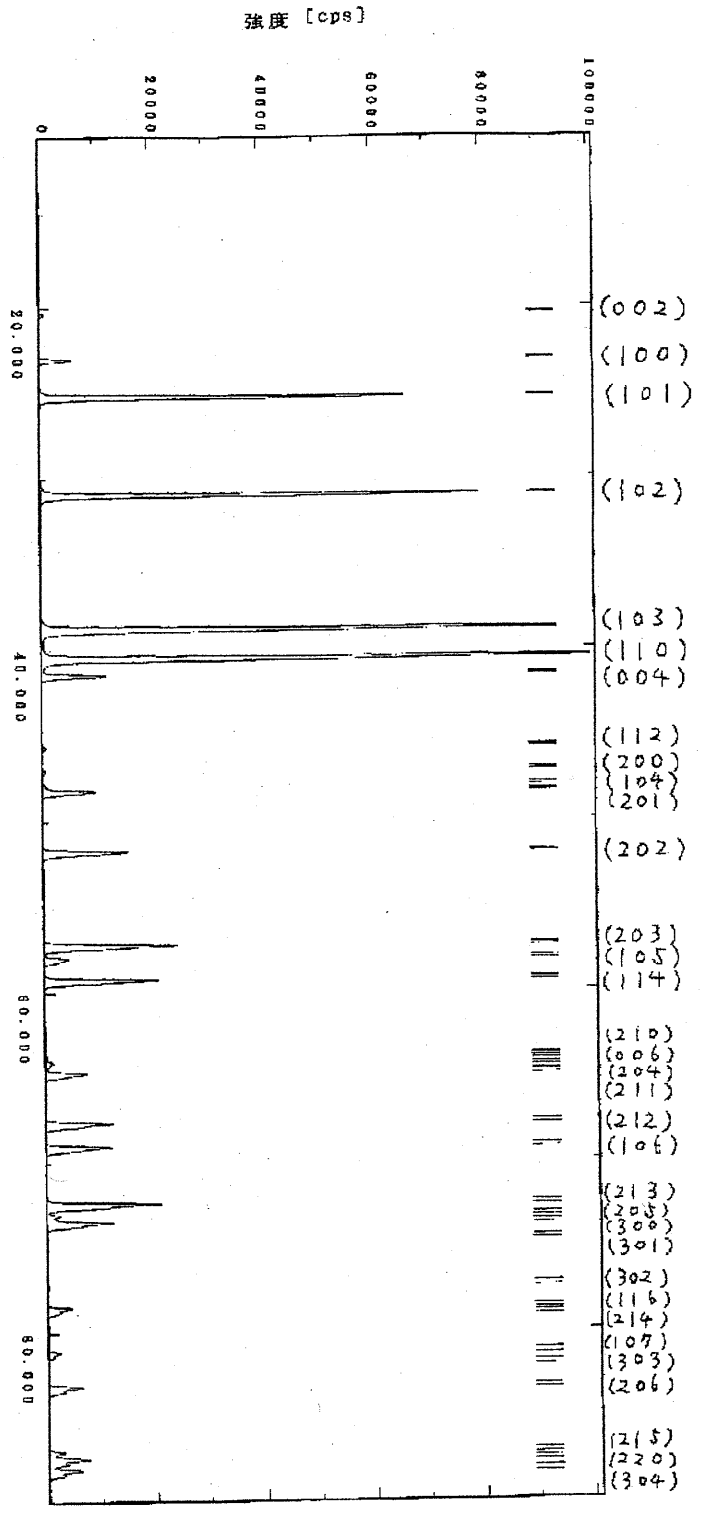

Figure 13: The position and intensity of diffraction peak for UCu_2Sn in Rietveld analysis. Numerical characters in parenthesis show the Miller index.

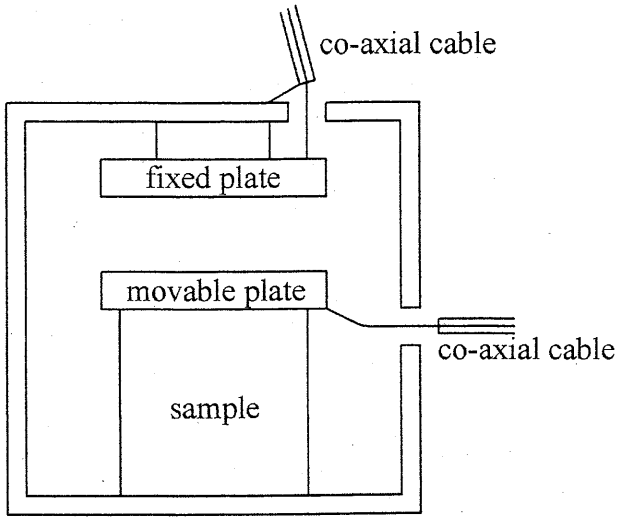

Figure 14: A diagram of the capacitance method.

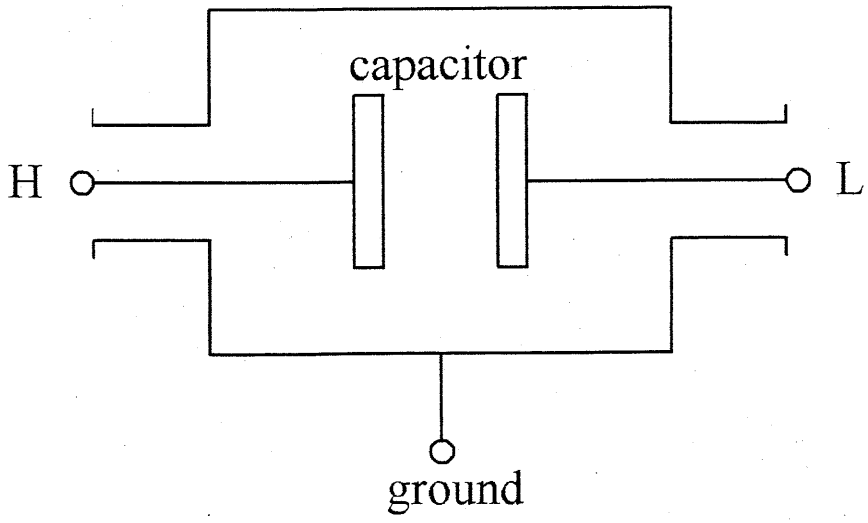

Figure 15: A diagram of the three-terminal method.

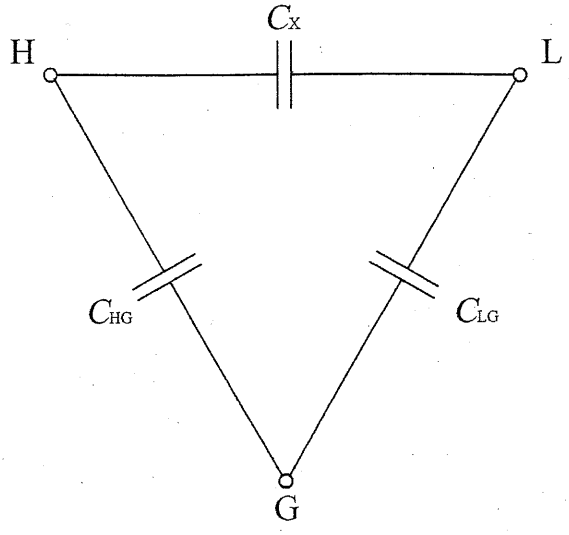

Figure 16: A equivalent circuit of the three-terminal method.

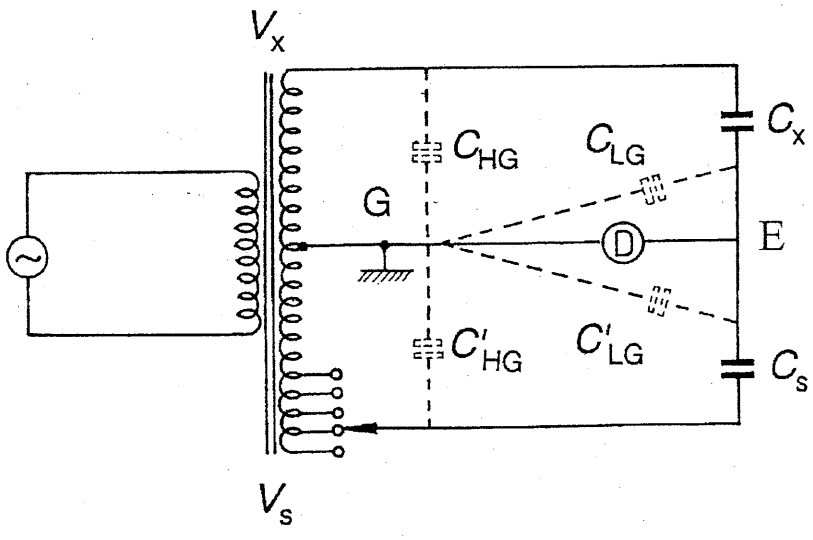

Figure 17: A diagram of bridge circuit for the three-terminal method.

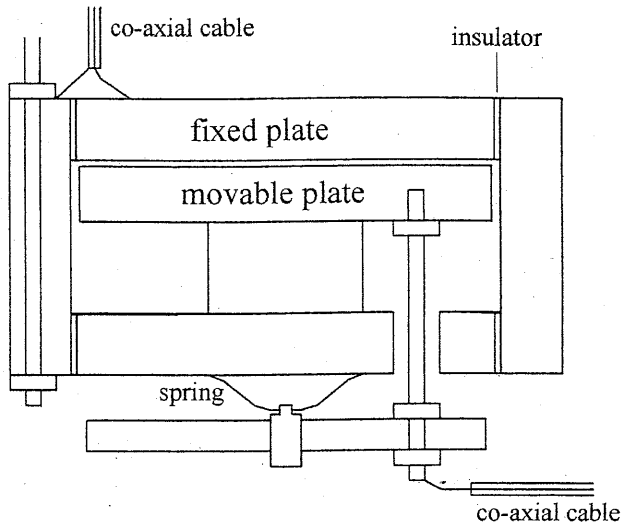

Figure 18: The structure of capacitance cell which is used for our experiments.

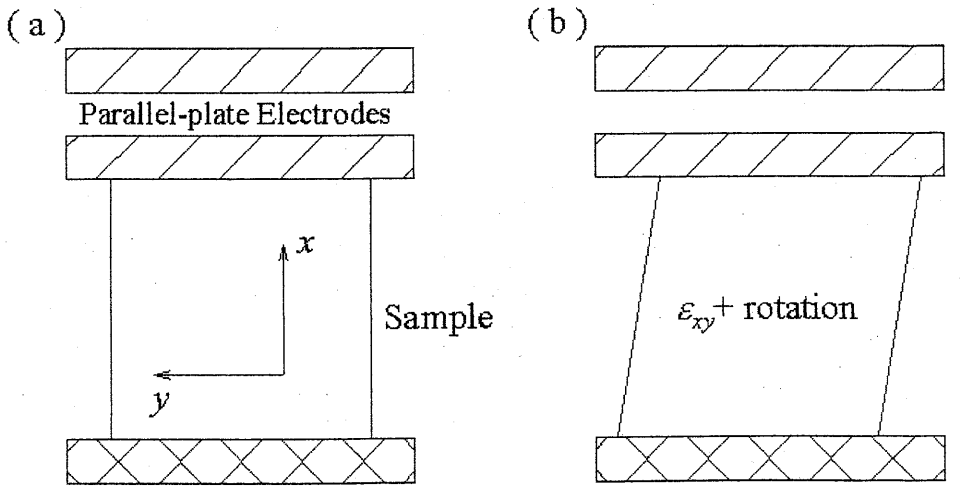

Figure 19: (a) Schematic illustration of the experimental setup for the capacitance measurement. In this configuration, we can measure the change in the length along the x direction. (b) Experimental setup for measuring e_{xy} across T_{Q}.

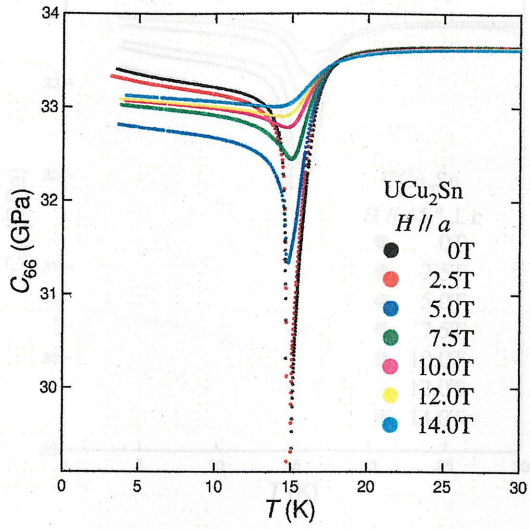

Figure 20: Temperature dependence of C_{66} in the magnetic field parallel to [100].

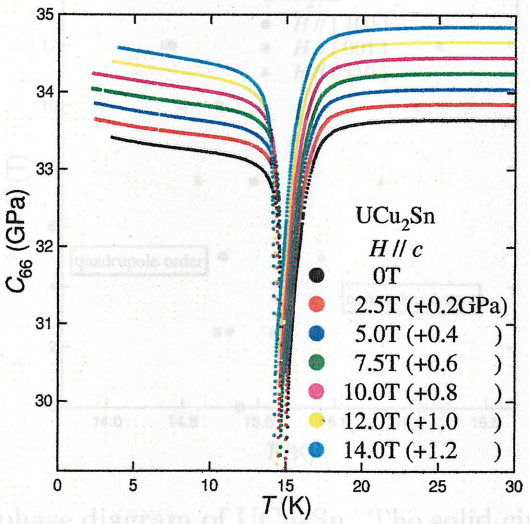

Figure 21: Temperature dependence of C_{66} in the magnetic field parallel to [001].

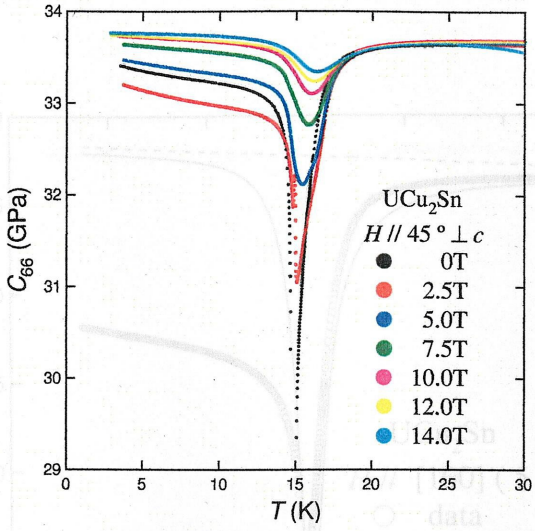

Figure 22: Temperature dependence of C_{66} in the magnetic field parallel to [110].

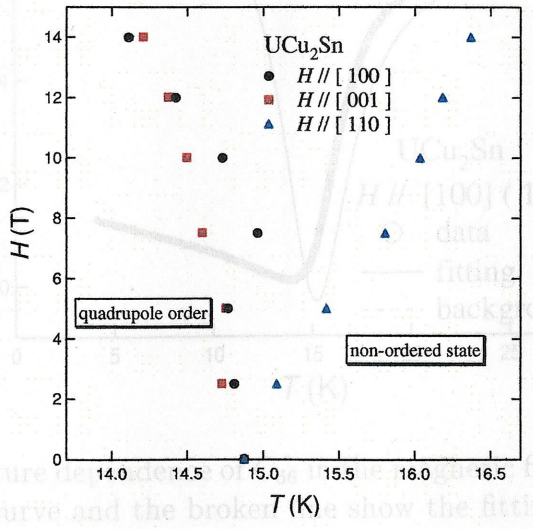

Figure 23: The H-T phase diagram of UCu_2Sn. The solid circles, squares and triangles show the transition temperature T_Q in H // [100], [001] and [110], respectively assuming that T_Q is the minimum point of data.

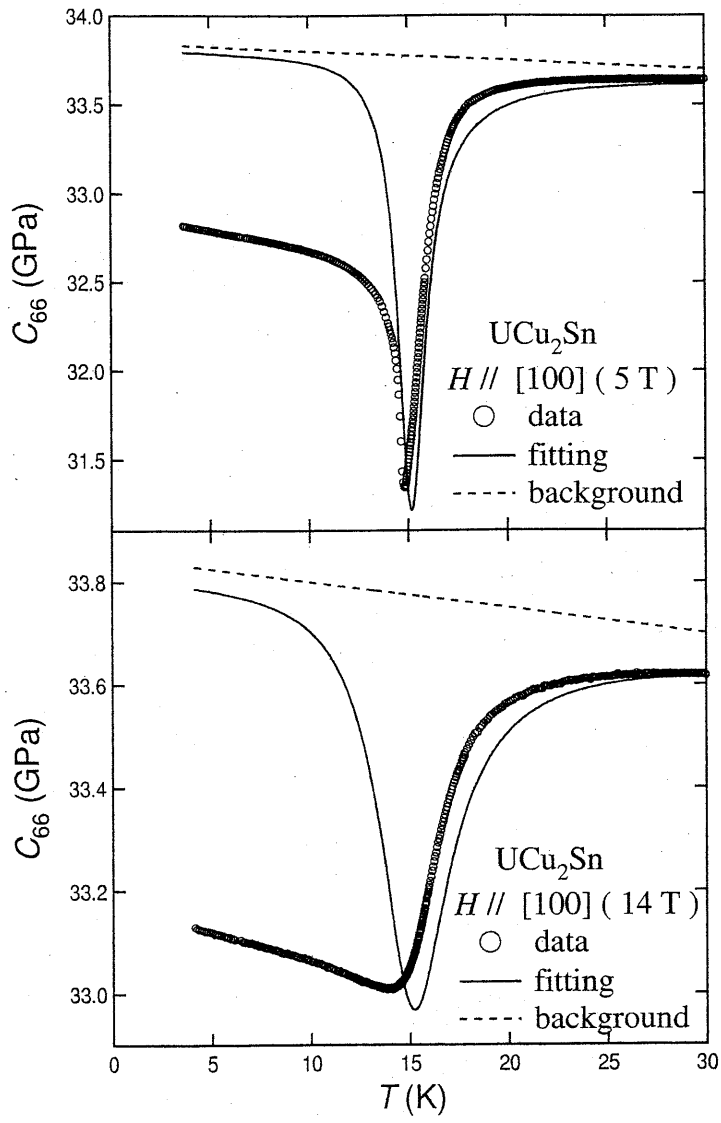

Figure 24: Temperature dependence of C_{66} in the magnetic field $H = 5, 14$ T parallel to [100]. The solid curve and the broken line show the fitting and the back ground stiffness, respectively.

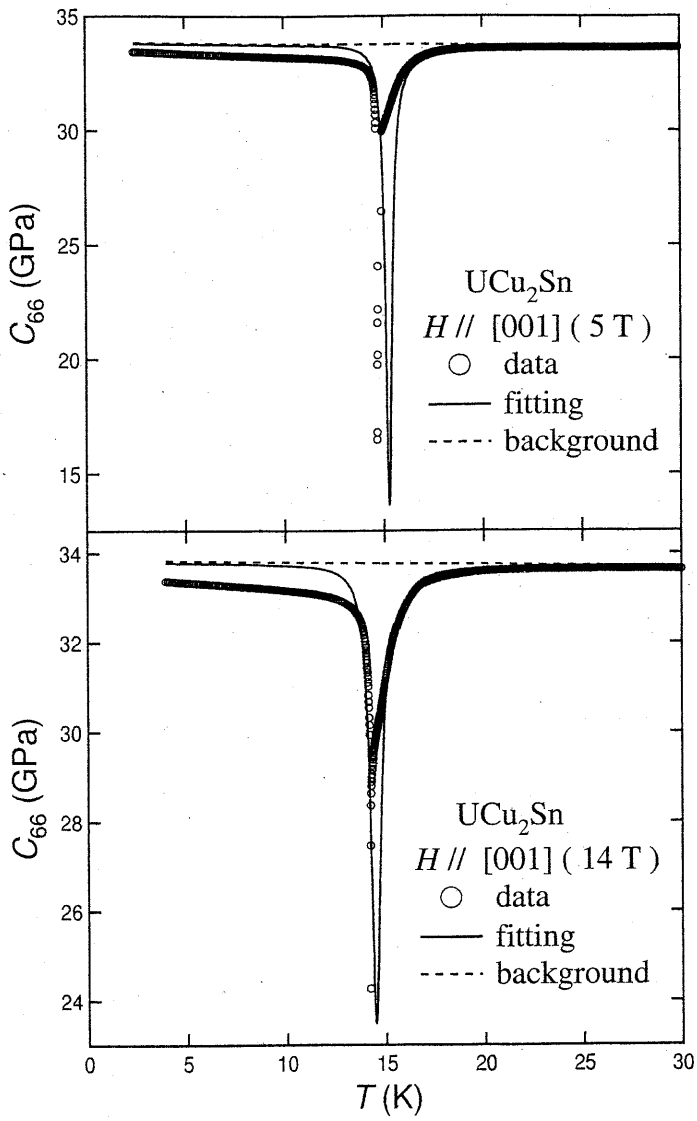

Figure 25: Temperature dependence of C_{66} in the magnetic field $H = 5, 14$ T parallel to [001]. The solid curve and the broken line show the fitting and the back ground stiffness, respectively.

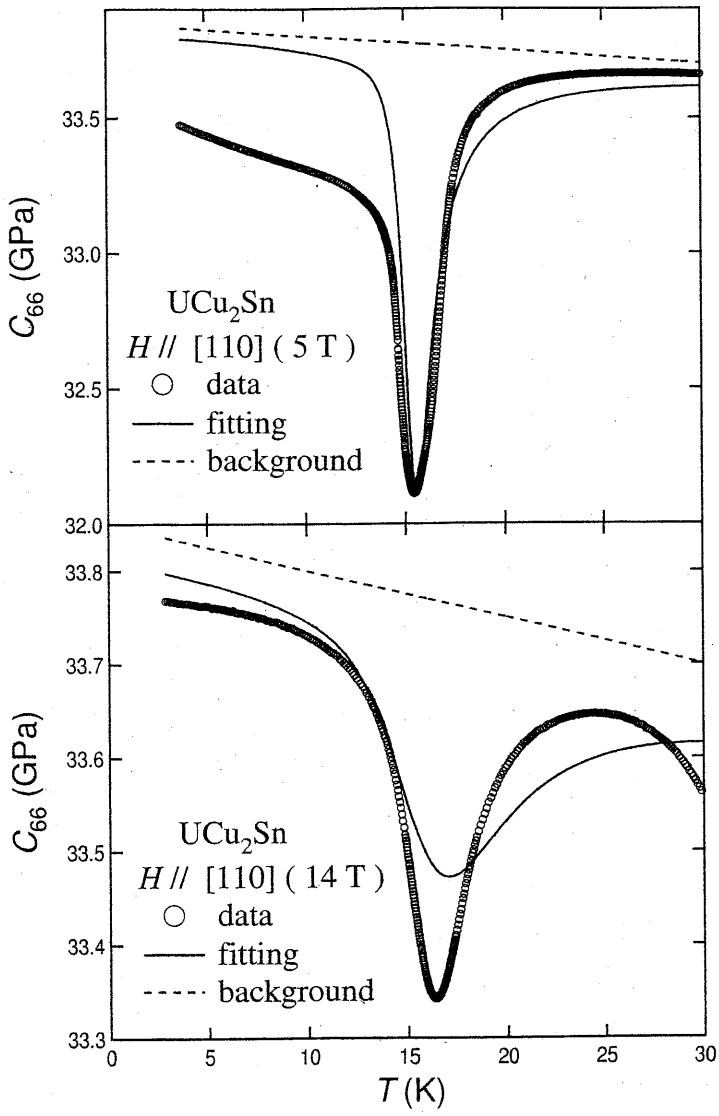

Figure 26: Temperature dependence of C_{66} in the magnetic field $H = 5, 14$ T parallel to [110]. The solid curve and the broken line show the fitting and the back ground stiffness, respectively.

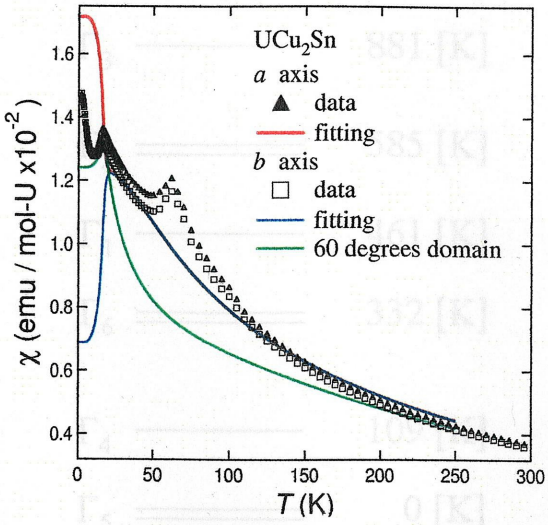

Figure 27: The magnetic susceptibility of UCu_2Sn along a and b axes are shown by open circles and solid triangles, respectively. The red and blue solid curves show the fitting result with CEF along a and b axes, respectively. The green solid curve shows the theoretical curve assumed for equally probability 60 degree domain structure.

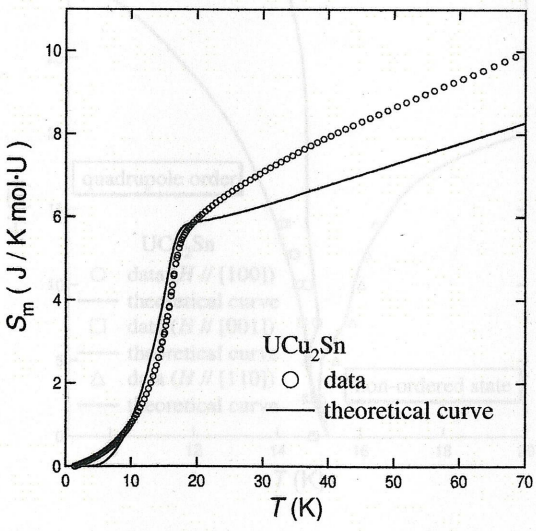

Figure 28: The magnetic entropy of UCu_2Sn derived from $5f$ electrons. The solid curve shows the entropy calculated by CEF parameters.

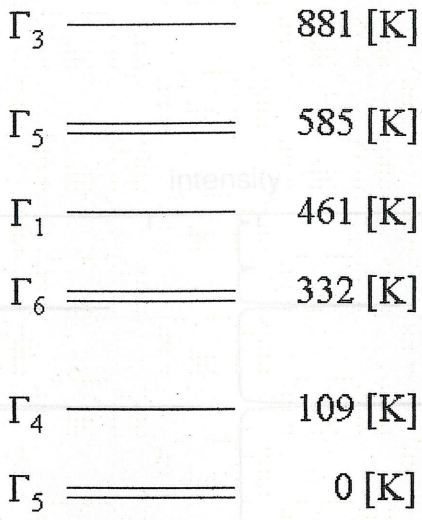

Figure 29: The CEF level scheme corresponding to CEF parameters in Table 1.

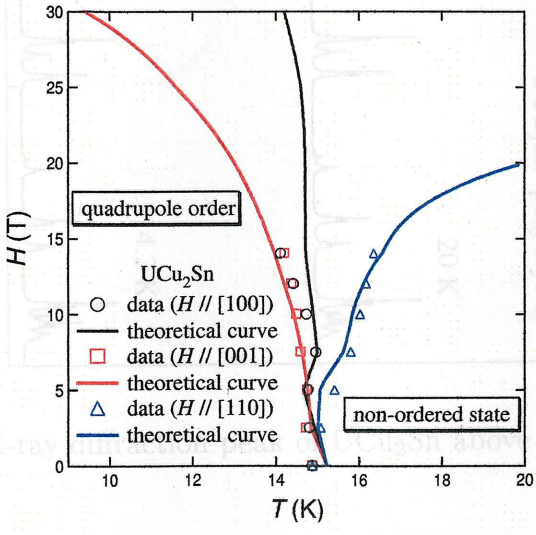

Figure 30: The H-T phase diagram of UCu_2Sn. Solid curves show theoretical curves calculated by fitting parameters.

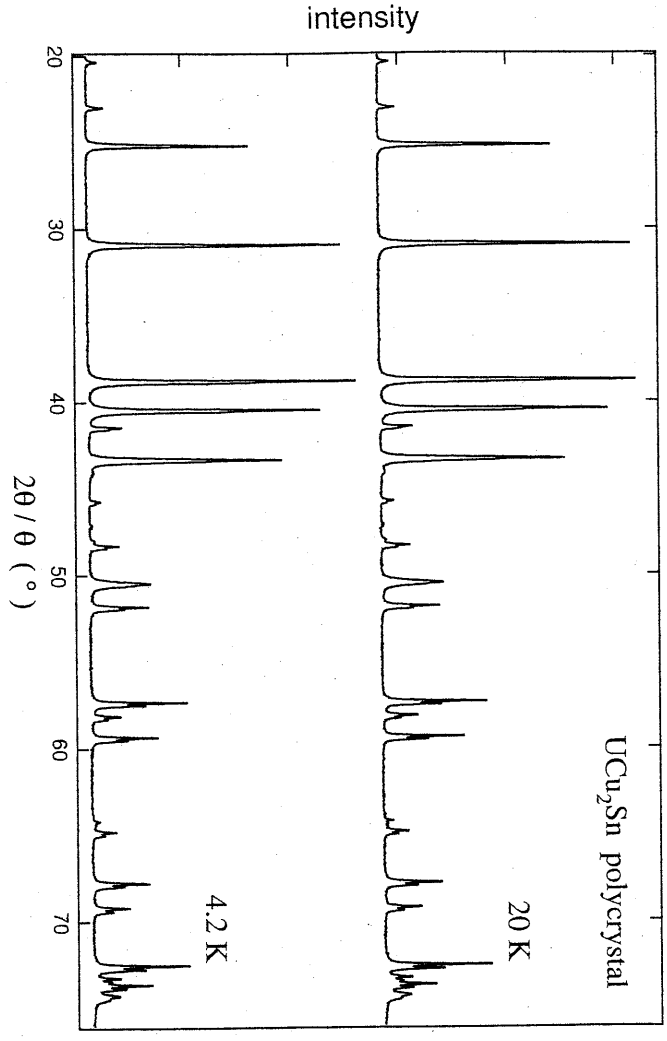

Figure 31: X-ray diffraction peak of UCu_2Sn above and below T_Q.

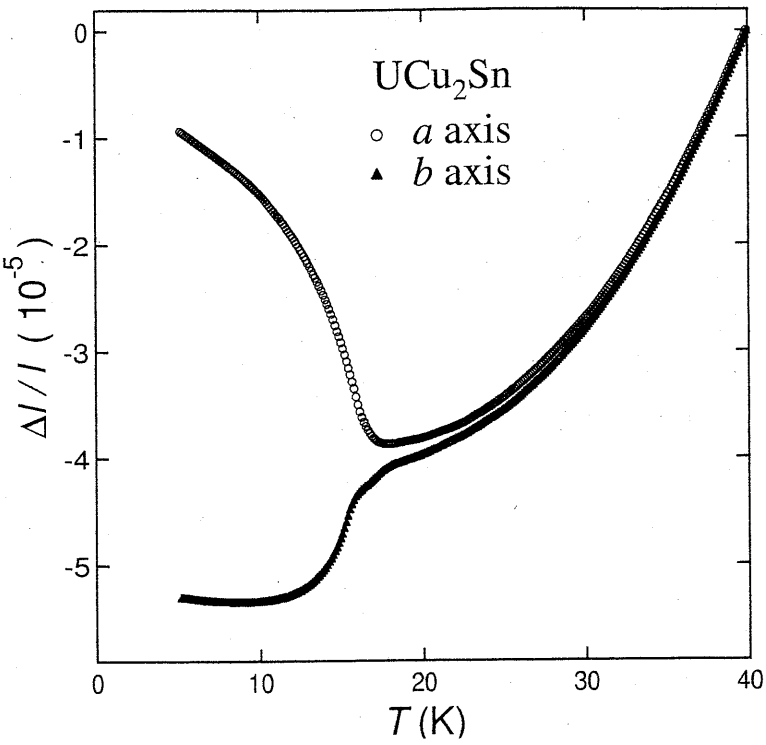

Figure 32: Temperature dependence of thermal expansion $\Delta l/l$ along the a and b axes are shown by open circles and solid triangles, respectively.

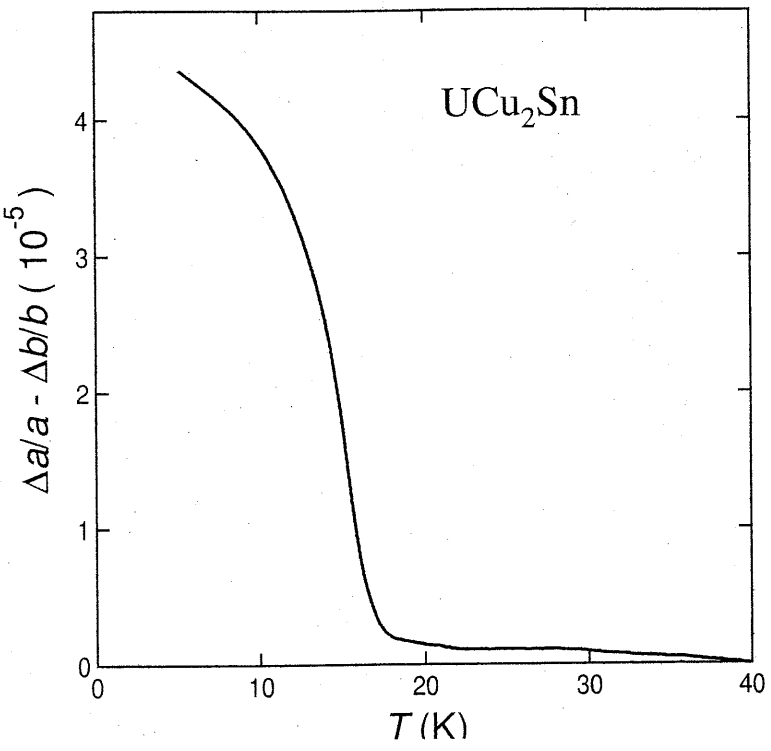

Figure 33: Temperature dependence of $\Delta a/a - \Delta b/b$.

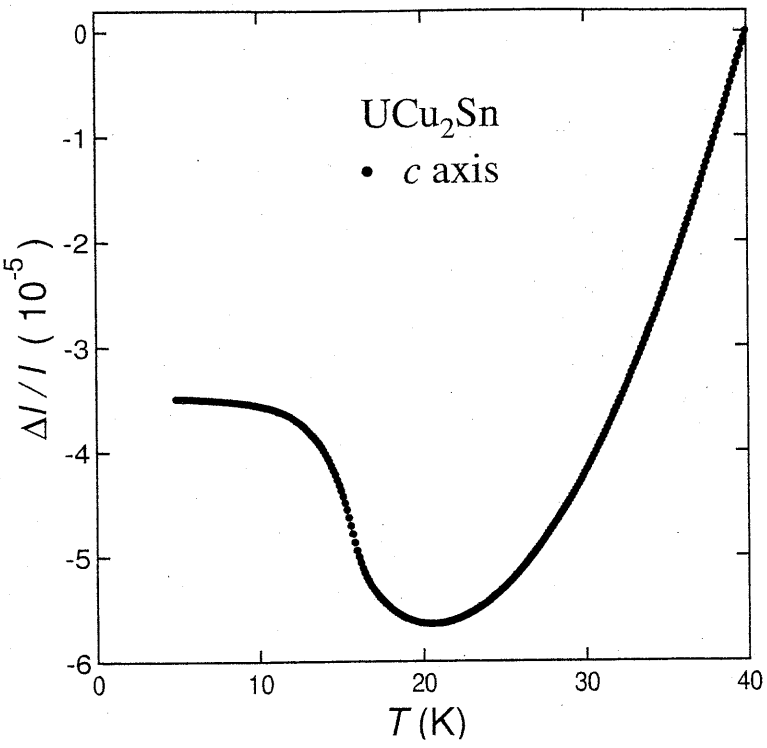

Figure 34: Temperature dependence of thermal expansion $\Delta l/l$ along the c axis.

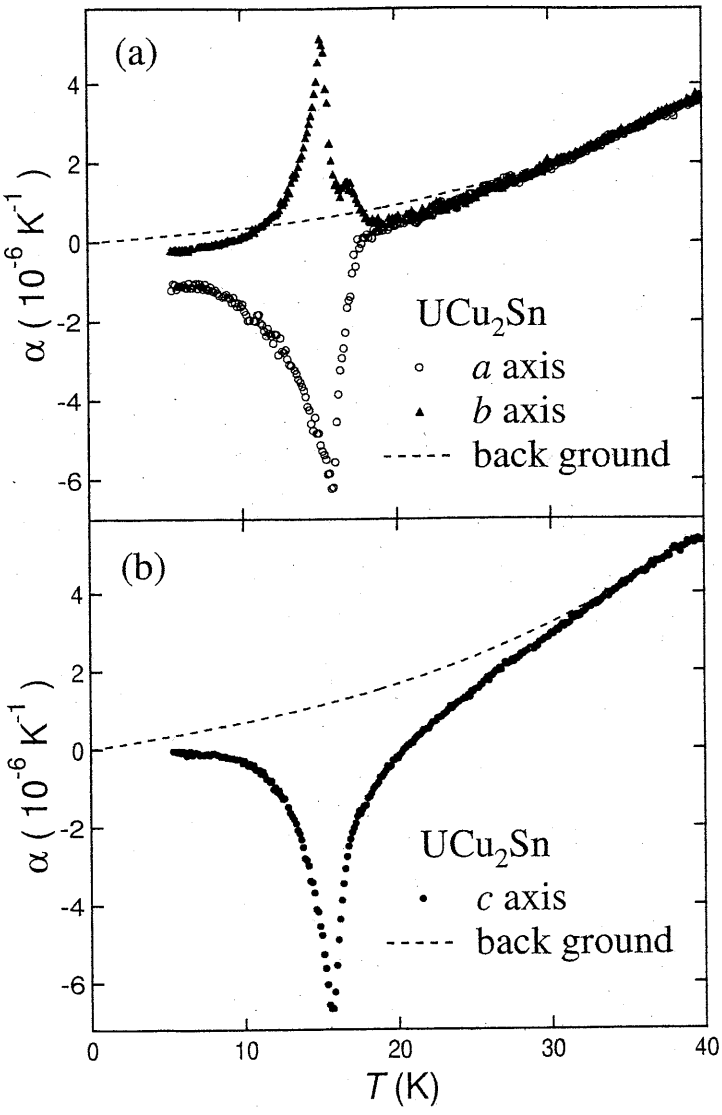

Figure 35: Temperature dependence of the thermal expansion coefficient $\alpha(T)$. (a) Open circles denote α measured along the a axis and solid triangles along the b axis. The broken curve indicates the background $\alpha_{\rm bg}$. (b) Solid circles denotes α along the c axis and the broken curve indicates the background.

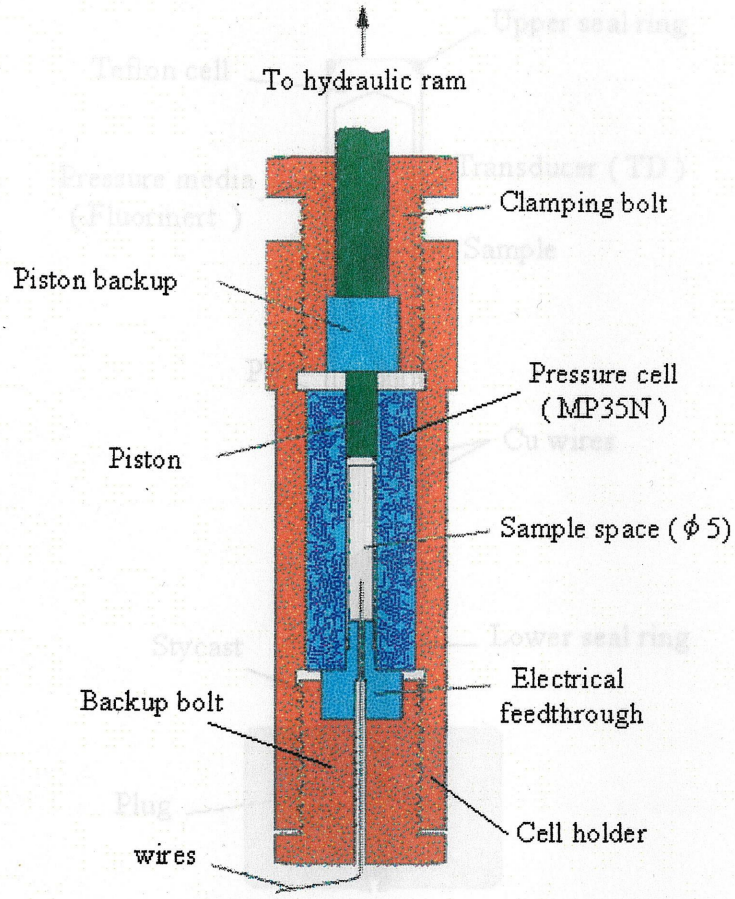

Figure 36: A diagram of the pressure cell for ultrasonic measurement.

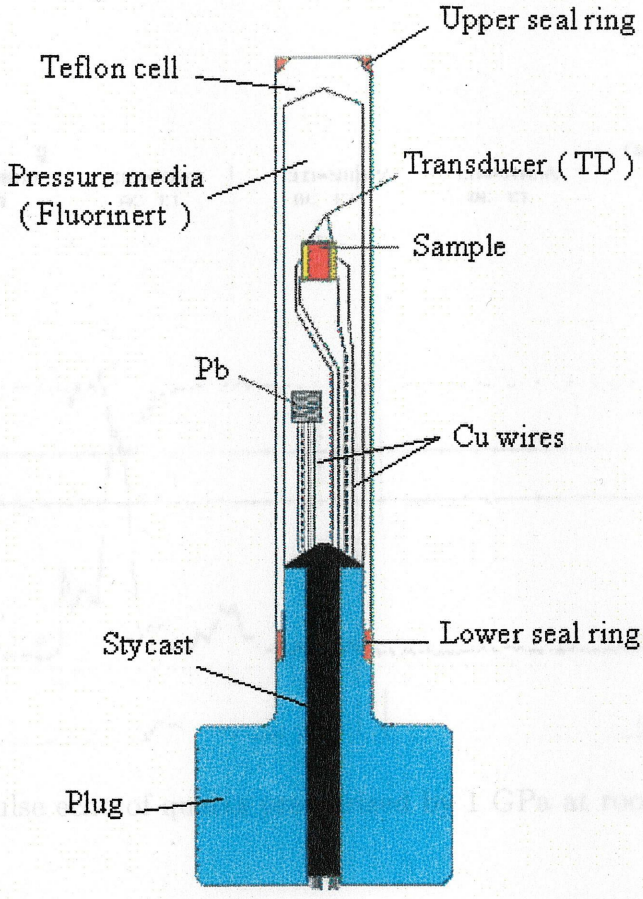

Figure 37: A diagram of the electrical feedthrough and sample space.

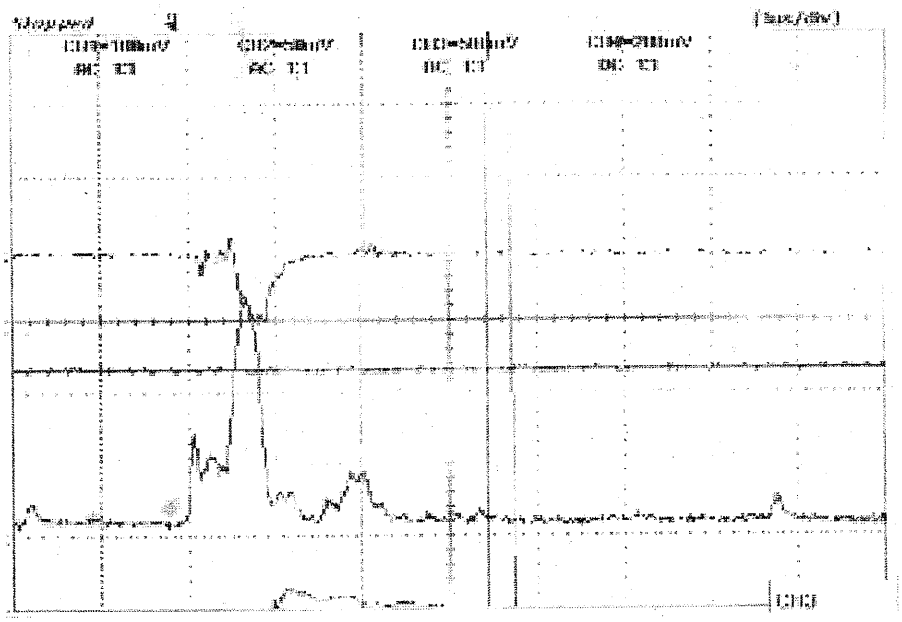

Figure 38: A pulse echo of quartz pressurized by 1 GPa at room temperature.

公表論文

(1) Spontaneous strain due to ferroquadrupolar ordering in UCu_2Sn

I. Ishii , H. Higaki , K. Katoh , T. Takabatake , H. Goshima , T. Fujita , T. Suzuki

Physical Review B **68**, 144413(4) (2003).

(2) Thermal expansion of UCu_2Sn in the basal plane

I. Ishii , H. Higaki , K. Katoh , T. Takabatake , H. Goshima , T. Fujita , T. Suzuki

Physica B **329-333**, 553-554 (2003).

参考論文

(1) Elastic anomaly of UCu_2Sn in the magnetic fields

T. Suzuki , I. Ishii , N. Okuda , K. Katoh , T. Takabatake , T. Fujita , A. Tamaki

Journal of Magnetism and Magnetic Materials **226-230**, 983-984 (2001).

(2) Quadrupolar ordering of 5*f* electrons in UCu_2Sn

T. Suzuki , I. Ishii , N. Okuda , K. Katoh , T. Takabatake , T. Fujita , A. Tamaki

Physical Review B **62**, 49-52 (2000).

(3) Jahn-Teller instability in a ternary uranium compound

T. Suzuki , I. Ishii , N. Okuda , K. Katoh , T. Takabatake , T. Fujita , A. Tamaki

Physica B **284-288**, 1301-1302 (2000).

(4) Elastic quantum oscillation of LuB_{12}

N. Okuda , T. Suzuki , I. Ishii , S. Hiura , F. Iga , T. Takabatake , T. Fujita ,

H. Kadomatsu , H. Harima

Physica B **281&282**, 756-757 (2000).